

Frequency-Dependent Characteristics of Regional Seismic Phases: Propagation of Pn in Western China

**Robert L. Nowack
Wang-Ping Chen**

**Purdue University
550 Stadium Mall Dr.
West Lafayette IN 47907**

Final Report

31 Jan 2011

APPROVED FOR PUBLIC RELEASE; DISTRIBUTION IS UNLIMITED.



**AIR FORCE RESEARCH LABORATORY
Space Vehicles Directorate
29 Randolph Rd
AIR FORCE MATERIEL COMMAND
HANSCOM AFB, MA 01731-3010**

NOTICES

Using Government drawings, specifications, or other data included in this document for any purpose other than Government procurement does not in any way obligate the U.S. Government. The fact that the Government formulated or supplied the drawings, specifications, or other data does not license the holder or any other person or corporation; or convey any rights or permission to manufacture, use, or sell any patented invention that may relate to them.

This report was cleared for public release and is available to the general public, including foreign nationals. Qualified requestors may obtain copies of this report from the Defense Technical Information Center (DTIC) (<http://www.dtic.mil>). All others should apply to the National Technical Information Service.

AFRL-RV-HA-TR-2011-1006 HAS BEEN REVIEWED AND IS APPROVED FOR PUBLICATION IN ACCORDANCE WITH ASSIGNED DISTRIBUTION STATEMENT.

//signature//

ROBERT J. RAISTRICK
Contract Manager

//signature//

JILL PARKER, Maj, USAF, Acting Chief
Battlespace Surveillance Innovation Center

This report is published in the interest of scientific and technical information exchange, and its publication does not constitute the Government's approval or disapproval of its ideas or findings.

REPORT DOCUMENTATION PAGE				Form Approved OMB No. 0704-0188	
Public reporting burden for this collection of information is estimated to average 1 hour per response, including the time for reviewing instructions, searching existing data sources, gathering and maintaining the data needed, and completing and reviewing this collection of information. Send comments regarding this burden estimate or any other aspect of this collection of information, including suggestions for reducing this burden to Department of Defense, Washington Headquarters Services, Directorate for Information Operations and Reports (0704-0188), 1215 Jefferson Davis Highway, Suite 1204, Arlington, VA 22202-4302. Respondents should be aware that notwithstanding any other provision of law, no person shall be subject to any penalty for failing to comply with a collection of information if it does not display a currently valid OMB control number. PLEASE DO NOT RETURN YOUR FORM TO THE ABOVE ADDRESS.					
1. REPORT DATE (DD-MM-YYYY) 31-01-2011		2. REPORT TYPE Final Report		3. DATES COVERED (From - To) 04-20-2008 to 12-31-2010	
4. TITLE AND SUBTITLE Frequency-dependent Characteristics of Regional Seismic Phases: Propagation of Pn in Western China				5a. CONTRACT NUMBER FA8718-08-C-0025	
				5b. GRANT NUMBER	
				5c. PROGRAM ELEMENT NUMBER 62601F	
6. AUTHOR(S) Robert L. Nowack ¹ and Wang-Ping Chen ²				5d. PROJECT NUMBER 1010	
				5e. TASK NUMBER SM	
				5f. WORK UNIT NUMBER A1	
7. PERFORMING ORGANIZATION NAME(S) AND ADDRESS(ES) Purdue University 550 Stadium Mall Dr. West Lafayette, IN 47907				8. PERFORMING ORGANIZATION REPORT NUMBER	
9. SPONSORING / MONITORING AGENCY NAME(S) AND ADDRESS(ES) Air Force Research Laboratory 29 Randolph Rd. Hanscom AFB, MA 01731-3010				10. SPONSOR/MONITOR'S ACRONYM(S) AFRL/RVBYE	
				11. SPONSOR/MONITOR'S REPORT NUMBER(S) AFRL-RV-HA-TR-2011-1006	
12. DISTRIBUTION / AVAILABILITY STATEMENT Approved for Public Release; Distribution Unlimited.					
13. SUPPLEMENTARY NOTES ¹ Dept of Earth and Atmospheric Sciences, Purdue University, West Lafayette, IN 47907 ² Dept of Geology, University of Illinois-Urbana, Urbana, IL 61801					
14. ABSTRACT The propagation of <i>Pn</i> waves has been investigated over a large region in western China using regional events recorded by the Hi-CLIMB array. Seismic attributes, including arrival times, Hilbert envelope amplitudes, and pulse frequencies, are modeled to investigate how velocity structures in the crust and the upper mantle affect the propagation of the <i>Pn</i> wave in Tibet. Travel-times are first modeled using 3D ray tracing to construct a 3D velocity model beneath the Hi-CLIMB array. The spectral element method, which provides complete numerical wave solutions in laterally varying media, was then used to model the seismic attribute data. Velocity and attenuation models beneath the Hi-CLIMB array are constructed and trade-offs between structural effects and attenuation are investigated. The objective of the study was to obtain self-consistent models of <i>Pn</i> propagation in western China free from assumptions such as a frequency-independent geometric spreading. To this end, our results should advance efforts in isolating effects of frequency-dependent propagation from those of pure-inelastic attenuation (<i>Q</i>), leading to improved methodologies for discrimination and yield estimates at regional distances.					
15. SUBJECT TERMS Regional Seismic Wave Propagation, Pn Waves, Hi-CLIMB array					
16. SECURITY CLASSIFICATION OF:			17. LIMITATION OF ABSTRACT	18. NUMBER OF PAGES	19a. NAME OF RESPONSIBLE PERSON
a. REPORT UNC	b. ABSTRACT UNC	c. THIS PAGE UNC			Robert Raistrick
			SAR	80	19b. TELEPHONE NUMBER (include area code) 781-377-3726

Table of Contents

1. Summary	1
2. Introduction	1
3. Travel-Time Modeling of Regional Events in Tibet	2
4. Spectral Element Modeling of the Pn Phase	6
5. Moment Tensors of Regional Events in Tibet	11
6. Specification of Moment Tensors for 2D SEM Modeling	14
7. Modeling of Pn Seismic Attributes in Tibet	15
8. Seismic Profiling with Teleseismic Waves	27
9. Conclusions	29
10. Recommendations	30
References	31
Appendix A. Calculation of Seismic Attributes	35
Appendix B. Validation of the Spectral Element Method for Pn Waves	37
Appendix C. Preprint of Paper by Griffin et al. (2011)	49
List of Symbols, Abbreviations, and Acronyms	72

Figures

1. Map of the stations of the Hi-CLIMB array in Tibet (triangles) and the epicenters of the selected regional earthquake sources (circles). Black circles are the hypocenters reports by the PDE catalogs and Engdahl et al. (1998), and the white circles are the epicenters nearest to the array that have been relocated in this study. The dashed lines indicate the locations of north-south slices of the P-wave velocities from travel-time modeling, with the East Line at 84 degrees, the Central Line at 85 degrees, and the West Line at 86 degrees in longitude. 2
2. Ray diagrams calculated using the 3D complete ray tracing code (CRT) for the Event L1E located by the dot. 3
3. These plots show the observed first-arrival travel times and the calculated travel times (lines and crosses) for the relocated nearby events using the average 1D crustal model on top and the refined crustal velocity model on the bottom. 4
4. These plots shows observed P-wave travel times (circles) and calculated travel times (lines and crosses) for the far-regional events, (A) L1e, (B) L1a, (C) L1i, (D) L1j, (E) L1k, and (F) E3b. The horizontal bars highlight the locations of the transition for shoaling of the Moho. 5
5. The 3D Moho and upper-mantle velocity structure found in this study for the region of the Hi-CLIMB array, with the left plot showing a view from the west and the right plot showing a view from the south. 5
6. North-south cross-sections of the 3D velocity model of Griffin et al. (2011) along longitudes of 84, 85 and 86 degrees. 6
7. The top plot shows the P-wave velocities for a simple layer over a gradient with an upper-mantle velocity gradient of .004 1/s. The bottom plot shows a simplified P-wave velocity model from travel-time modeling of regional events from Hi-CLIMB, showing a step in the Moho. 7
8. SEM synthetic P-wave A) travel-times, B) amplitudes and C) pulse centroid frequencies for a flat Moho with several velocity models with different upper-mantle velocity gradients of 0.0, 0.002, 0.004, and 0.006 1/s. For this case no Q is included. 8
9. SEM synthetic P-wave A) travel-times, B) amplitudes and C) pulse centroid frequencies for a flat Moho with several velocity models with different upper-mantle velocity gradients of 0.0, 0.002, 0.004, and 0.006 1/s. For this case a Q of 150 is assumed in the crust and 400 in the mantle. 9
10. SEM synthetic A) travel-times, B) amplitudes and C) pulse centroid frequencies for a step in the Moho, as shown for the right plot in Figure 7. The crosses for source B near 1000 km in Figure 7 (right plot) and recorded to the south, and the circles are for a source A near 0 km and recorded to the north in Figure 7 (right plot). 10
11. SEM synthetic A) travel-times, B) amplitudes and C) pulse centroid frequencies for a step in the Moho, as shown for the right plot in Figure 7. The crosses for source B near 1000 km in

Figure 7 (right plot) and recorded to the south, and the circles are for a source A near 0 km and recorded to the north in Figure 7 (right plot). 11

12. Inversion of three-component waveforms for the focal-mechanism of event E3b using data from the Hi-CLIMB array. The top right plot shows the data misfit with a narrow minimum at 6 km and a broad flat minimum at 19 km, and the upper left plot shows the 19 km solution. The lower plots show the matches between the observed and calculated waveform data. 12

13. Focal mechanism solutions for Event E3b. a) A comparison global CMT focal mechanism for an earthquake located about 70 km distant from Event E3b. b) The focal mechanism solution for Event E3b with a data misfit minimum at a depth of 6 km. c) The focal mechanism solution for Event E3b with a data misfit minimum at a depth of 19 km. d) The focal mechanism for Event E3b for a shift in epicenter of 10 km to the east resulting in a least misfit minimum at the shallower depth of 7 km. All solutions indicate East-West extension. 13

14. The left plot shows the 3D focal mechanism for a particular double-couple moment tensor source with four angles given by dashed lines. The P_g and P_n take-off angles are shown by small circles. The right plot shows the amplitudes on the focal sphere of the 2D moment tensor for the azimuthal angles given in the left plot as a function of take-off angle derived from the 3D moment tensor. 14

15. The left plot shows a focal mechanism with four azimuthal angles given by dashed lines. The P_n and P_g take-off angles are shown by the small circles. The right plot shows the SEM envelope amplitudes for the azimuthal angles given on the left. Different symbols represent different azimuthal angles. 15

16. The left map shows the original and slightly revised focal mechanism for event L1E. The middle map shows the focal mechanism TL-1 and an alternative focal mechanism TL-2 for event E3B. The right map shows the focal mechanisms for the cluster of south events L1A, L1I, L1J, and L1K. The triangles show the Hi-Climb stations, where the solid triangles along with the solid lines show the orientation angles used for the specification of the moment tensor. The dashed lines show the separation of ranges used to specify the moment tensor. 15

17. This map shows the location where 2D P-wave velocity slices were obtained from 3D velocity model of Griffin et al. (2011). Triangles represent the Hi-Climb array. The circles show the events used by Griffin et al. (2011) for the 3D velocity model where the open circles are relocations. The dashed lines show the West, Central, and East lines for the 2D slices. 16

18. The plots show the P-velocities for 3 different slices of the 3D model of Griffin et al. (2011) which constant upper mantle velocity gradients but different upper mantle top velocities. The small circles show location of the events used with each velocity slice. 17

19. These plots show the calculated travel-times of the selected events with no attenuation in the SEM models compared with the observed travel-times. Circles are the SEM calculated travel-times and crosses are observed travel-times. 18

20. These plots show the peak envelope amplitudes of the selected events with no attenuation in the SEM models compared with the observed envelope amplitudes. The circles are the SEM

calculated values and the crosses are observed envelope amplitudes. The distance ranges for the specified orientation angles for the moment tensor are also shown. For event L1E, the modified moment tensor is used and for event E3B the TL-1 moment tensor is shown. 19

21. These plot show the calculated instantaneous pulse frequencies of the selected events with no attenuation for the SEM models compared with the observed instantaneous and pulse frequencies. The circles are the SEM calculations and the crosses and squares are the observed instantaneous and centroid frequencies. For event L1E, the modified moment tensor is used and for event E3B the TL-1 moment tensor is shown. 20

22. These plots show variable upper mantle Q models for each slice determined from modeling seismic attributes from the selected regional events assuming the velocity slices in Figure 18. 21

23. These plot show the SEM calculated peak envelope amplitudes of the selected events with the attenuation models shown in Figure 22 and the velocity slices given in Figure 18 compared with the observed envelope amplitudes. The circles are the SEM calculated values and the crosses are observed envelope amplitudes. The distance ranges for the specified orientation angles for the moment tensor are also shown. For event L1E, the modified moment tensor is used and for event E3B the TL-1 moment tensor is shown. 22

24. These plot show the SEM calculated pulse frequencies of the selected events with the attenuation models shown in Figure 22 and the velocity slices given in Figure 18 compared with the observed pulse frequencies. The circles are the SEM calculations and the crosses and squares are the observed instantaneous and centroid frequencies. For event L1E, the modified moment tensor is used and for event E3B the TL-1 moment tensor is shown. 23

25. The plots show the P-velocities for 3 different slices of the 3D model of Griffin et al. (2011) which variable upper mantle velocity gradients. The small circles show location of the events used with each velocity slice. 24

26. The plots shows constant upper mantle attenuation used with the velocity models in Figure 25 with a laterally variable upper mantle velocity gradient between the Lhasa and Qiangtang terranes. 25

27. These plots show the peak envelope amplitudes of the selected events with a constant attenuation in the upper mantle for the SEM models compared with the observed envelope amplitudes. The circles are the SEM calculations and the crosses are observe envelope amplitudes. 26

28. These plots show the instantaneous pulse frequencies of the selected events with a constant attenuation and a variable upper mantle velocity gradient for the SEM models compared with the observed instantaneous and centroid frequencies. The circles are the SEM calculations and the crosses and squares are observed instantaneous and centroid frequencies. 27

29. North-south trending profile across southern and central Tibet, showing topography on top, a P-wave reflection profile constructed using the phase SsPmp, and the estimated crustal thickness (Panels a, b, c, respectively). 28

30. A comparison between crustal thickness estimated from wide-angle P-wave reflections (dots) from the teleseismic *SsPmp* phase and an image of the Tibetan lithosphere obtained from Gaussian beam migration of direct P- to S-wave conversions (from Tseng et al., 2009; and the Gaussian beam migration from Nowack et al., 2010). 29
- A.1. This shows an example of a data trace from the Hi-CLIMB array with a window function at the top and a windowed trace and envelope at the bottom. 32
- B.1. Source time functions for the reflectivity calculation (solid line) with $\tau = 0.2$ sec and the SEM calculation with $\alpha_0 = 7.4$ (dashed line). 34
- B.2. SEM synthetics of model Moho-1 with no 3D correction (top) and SEM synthetics of model Moho-1 with 3D distance and pulse shape corrections (bottom). Top and bottom amplitudes are scaled by the maximum amplitude of all traces. 39
- B.3. A comparison between the SEM calculations (dashed) and the reflectivity results (solid) of Braile and Smith (1975) for a constant velocity 30 km crust over a constant velocity mantle. The amplitudes of the reflectivity results and the 3D corrected SEM results are both multiplied by distance in the plot. 40
- B.4. A comparison between the results from the SEM calculations (dashed) and the reflectivity results (solid) of Braile and Smith (1975) for a constant velocity 30 km crust over a mantle with a velocity gradient in the top 5 km. Amplitudes of the reflectivity results and the corrected SEM results are both multiplied by distance in the plot. 41
- B.5. This shows a comparison between the SEM calculations (crosses) and the asymptotic calculations (background plot) of Cerveny and Ravindra (1971) for the pure and interference head waves. C^+ wave is the interference head wave, C_0 is the diving wave, and the 131 wave is the pure head wave case (Modified background plot from Cerveny and Ravindra, 1971). 42
- B.6. This shows amplitude spectra as a function of distance for the interference head wave case. The thin black curves are from Cerveny and Ravindra (1971) and the thicker curves are from SEM calculations for the same model (Background plot from Cerveny and Ravindra, 1971). 43
- B.7. This shows the comparison of the SEM traces with the analytical calculations for a homogeneous viscoelastic model with a Q_p of 112.5. 44
- B.8. This shows the envelope amplitude of the SEM traces with the envelope amplitude of the analytically calculated traces given in figure B.7. 45
- B.9. This shows a comparison of the frequency spectra of the SEM traces with analytical calculations for the traces given in figure B.7. 45

Acknowledgments

Seismic data used in this study were collected as part of the Hi-CLIMB project using instrumentation from different sources, including many stations from the Incorporated Research Institutions in Seismology – Program for the Array Seismic Studies of the Continental Lithosphere (IRIS – PASCAL) Center. The original Hi-CLIMB field project was organized and coordinated jointly by the University of Illinois (Principal Investigator, Wang-Ping Chen) and Oregon State University (Principal Investigator, John Nabelek) (Nabelek et al., 2005). Seismic data from this experiment can be directly obtained from the IRIS Data Management Center at www.iris.edu.

We would like to thank Dimitri Komatitsch of the University of Toulouse, France for his assistance in addressing issues related to implementation of the spectral element method. The spectral element code Specfem 2D is available at <http://www.geodynamics.org/cig/software>. We would also like to thank the SW3D (Seismic Waves in Complex 3-D Structures) consortium at Charles University in Prague for providing updates of the 3D ray tracing code CRT (Complete Ray Tracing) from <http://sw3d.mff.cuni.cz/software/index.htm>.

The students at Purdue involved with the project were Jessica D. Griffin and Ali C. Bakir. The work was also partially supported by the U.S. National Science Foundation grants EAR06-35419 (W.-P. Chen and T.-L. Tseng), EAR06-35611 (R. L. Nowack), and the Geo-Mathematical Imaging Group (GMIG) at Purdue University.

1. SUMMARY

The propagation of Pn waves has been investigated over a large region in western China using regional events recorded by the Hi-CLIMB array. Seismic attributes, including arrival times, Hilbert envelope amplitudes, and pulse frequencies, are modeled to investigate how velocity structures in the crust and the upper mantle affect the propagation of the Pn wave in Tibet. Travel-times are first modeled using 3D ray tracing to construct a 3D velocity model beneath the Hi-CLIMB array. The spectral element method, which provides complete numerical wave solutions in laterally varying media, was then used to model the seismic attribute data. Velocity and attenuation models beneath the Hi-CLIMB array are constructed and trade-offs between structural effects and attenuation are investigated. The objective of the study was to obtain self-consistent models of Pn propagation in western China free from assumptions such as a frequency-independent geometric spreading. To this end, our results should advance efforts in isolating effects of frequency-dependent propagation from those of pure-inelastic attenuation (Q), leading to improved methodologies for discrimination and yield estimates at regional distances.

2. INTRODUCTION

Using seismic data from regional earthquakes recorded by the Hi-CLIMB array, we have investigated trade-offs between velocity structure and attenuation in Tibet. Of more than 30 high-quality, regional seismic profiles that have been assembled, we have selected 10 which show excellent crustal and P_n arrivals for further analysis. We first model P -wave arrival-times to constrain the velocity structure in the crust and the upper mantle in central and western Tibet. Travel-times from four events along the Hi-CLIMB array provide details on crustal velocities, and six events at regional distances to the array provide further constraints on Moho structure and upper mantle lid velocities. We use 3D ray tracing to model the travel-times, and the results indicate that both Moho structure and mantle-lid velocities in the region are three-dimensional in nature but approximately follow the trend of the Bangong-Nujiang Suture (BNS). Although only a limited number of events were used for the travel-time modeling, the results are consistent with earlier results from teleseismic imaging using the Hi-CLIMB array.

Attributes of the Pn waves, including envelope amplitudes and instantaneous frequencies (see Appendix A), are next modeled using the spectral element method (SEM) using regional earthquakes recorded by the Hi-CLIMB array in Tibet. Three 2D P -wave velocity slices for the events were used in the SEM calculations. All the slices are earth-flattened for use in the 2D SEM calculations, and the SEM results are then corrected for out-of-plane spreading.

The SEM modeling of the pulse amplitudes and frequencies suggests a variable upper mantle structure in which the Qiangtang terrane has higher attenuation than the Lhasa terrane in the upper mantle. However, the modeling with a constant upper mantle attenuation structure also shows that this can provide a good fit to the observed

amplitudes and frequencies, but only if a variable velocity gradient structure exists with a lower velocity gradient beneath the Qiangtang terrane compared to the Lhasa terrane.

From the observations and modeling of the seismic attributes in this study, two alternate models for the region are found, one with a constant upper mantle velocity gradient similar to those of Griffin et al. (2011) and Phillips et al. (2007) with a variable attenuation model and one with a constant attenuation model and a variable upper mantle velocity gradient similar to that of Myers et al. (2010). In either case, the upper mantle of the Qiangtang terrane can be distinguished from the Lhasa terrane. The lower P_n velocities, and lower P_n amplitudes, suggest hotter temperatures in the upper mantle beneath the Qiangtang terrane in the north compared to the Lhasa terrane. Either lower Q_p values or a lower upper mantle velocity gradient in the Qiangtang terrane compared to the Lhasa terrane can be used to match the seismic attribute data presented here.

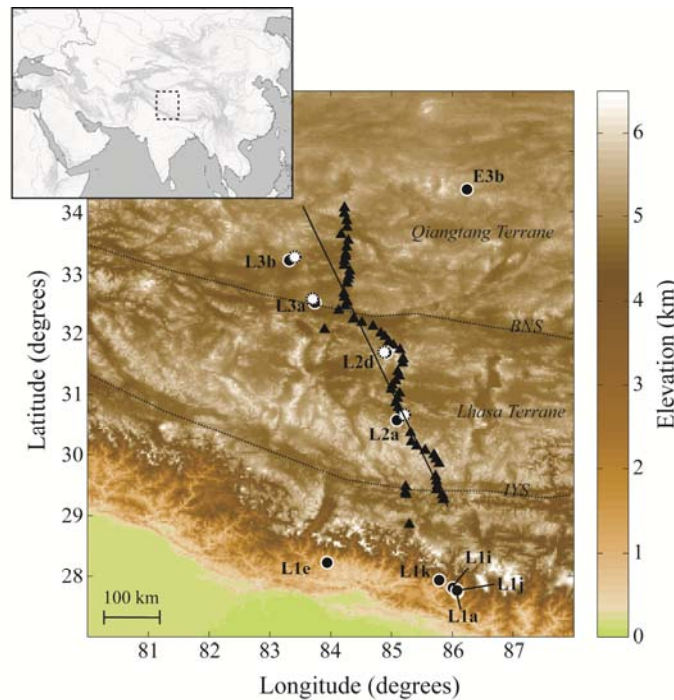


Figure 1. Map of the stations of the Hi-CLIMB array in Tibet (triangles) and the epicenters of the selected regional earthquake sources (circles). Black circles are the hypocenters reports by the PDE catalogs and Engdahl et al. (1998), and the white circles are the epicenters nearest to the array that have been relocated in this study. The dashed lines indicate the locations of north-south slices of the P-wave velocities from travel-time modeling, with the East Line at 84 degrees, the Central Line at 85 degrees, and the West Line at 86 degrees in longitude.

3. TRAVEL-TIME MODELING OF REGIONAL EVENTS IN TIBET

Regional events recorded by the Tibetan Hi-CLIMB array with locations approximately in-line with the array have been chosen for analysis here and are shown in Figure 1. However, other events in specific terranes have also been identified for later

processing. Four of the in-line events have epicenters less than 200 km from the Hi-CLIMB array, and these events were relocated with data from the Hi-CLIMB array using the earthquake location program HYPOINVERSE-2000 (Klein, 2002). The Engdahl et al. (1998) or the Preliminary Determination of Epicenters (PDE) catalogs were used for all event locations except the four nearby events (L2a, L2d, L3a, and L3b), which were relocated using Hi-CLIMB data.

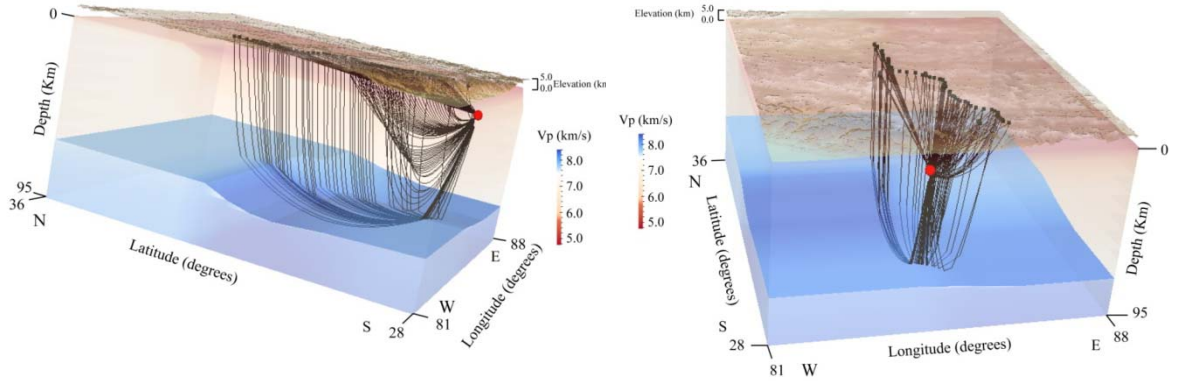


Figure 2. Ray diagrams calculated using the 3D complete ray tracing code (CRT) for the Event L1E located by the dot.

The relocations improved the fit to the travel-times but moved the epicenters on average about 5 km. For more distant events in Tibet, a focal depth normalization procedure was used since events on the Tibetan plateau are dominantly less than 15 km in focal depth (e.g., Molnar and Chen, 1983; Chen and Molnar, 1983; Langin et al., 2003).

Figure 2 shows ray diagrams calculated using the 3D complete ray tracing code CRT (Cerveny et al., 1988) for the Event L1e shown by the small circle. The left plot is viewed from the west, and the right plot is viewed from the south. The blue top surface indicates the structure of the Moho used for the 3D model. The top plot of Figure 3 shows the observed P-wave travel times for the relocated nearby events L2a, L2d, L3a, and L3b, compared with the calculated travel times using an average 1D crustal velocity model. The bottom plot of Figure 3 shows the observed travel times of the first-arrival P waves for the nearby events, compared with the calculated travel times of a refined, laterally varying crustal velocity model. Figure 4 shows the observed P-wave travel-times (circles) for the far-regional Events (A) L1e, (B) L1a, (C) L1i, (D) L1j, (E) L1k, and (F) E3b. The *P_n* travel-times for these events were used to constrain the Moho structure and *P*-wave velocities in the upper mantle for this part of the Tibetan Plateau. The lines and crosses in each of the far-regional travel-time plots are the calculated travel-times using the inferred 3D regional velocity model.

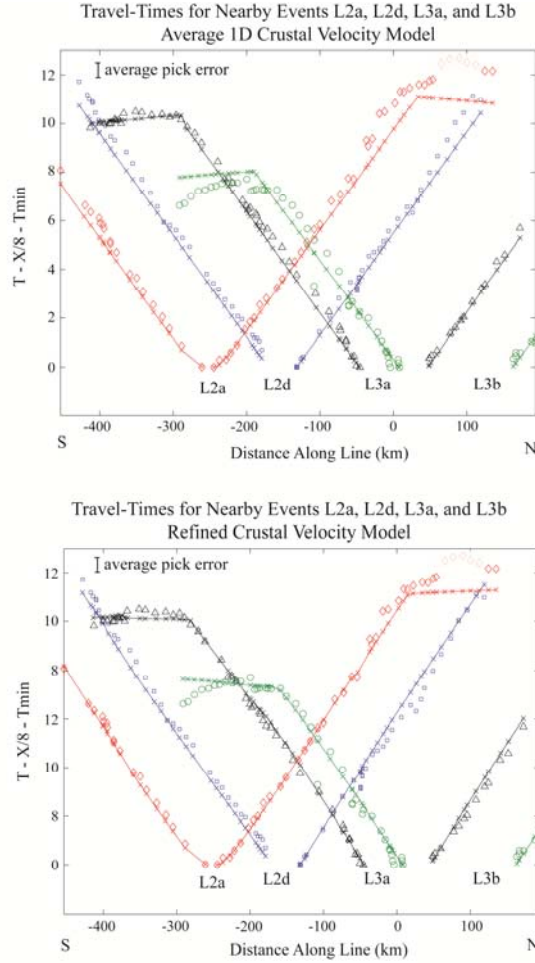


Figure 3. These plots show the observed first-arrival travel times and the calculated travel times (lines and crosses) for the relocated nearby events using the average 1D crustal model on top and the refined crustal velocity model on the bottom.

Figure 5 shows plots of the 3D Moho and upper-mantle velocity structure found in this study from the modeling of near and far regional travel-time data for this region of the Tibetan Plateau, as viewed from (A) the west and (B) the south (Griffin et al., 2011). The upper-mantle velocities are higher and the Moho deeper beneath the southern portion of the plateau south of the Bangong-Nuijiang suture (BNS), and upper-mantle velocities are lower and the Moho is shallower north of the BNS. North-south cross-sections of the 3D velocity model of Griffin et al. (2011) are shown in Figure 6 for longitudes of 84, 85 and 86 degrees.

The structural results from Griffin et al. (2011) based on the modeling of the travel-time modeling of regional events are similar to those found by Tseng et al. (2009) using virtual seismic profiles from *SsPmP* teleseismic waves and by Nowack et al. (2010) using Gaussian beam migration of teleseismic receiver functions. Other structure controls on the structure have been found by Hung et al. (2010) using finite frequency tomography of teleseismic arrival times, and for anisotropic structure of the upper mantle by Chen et al. (2010).

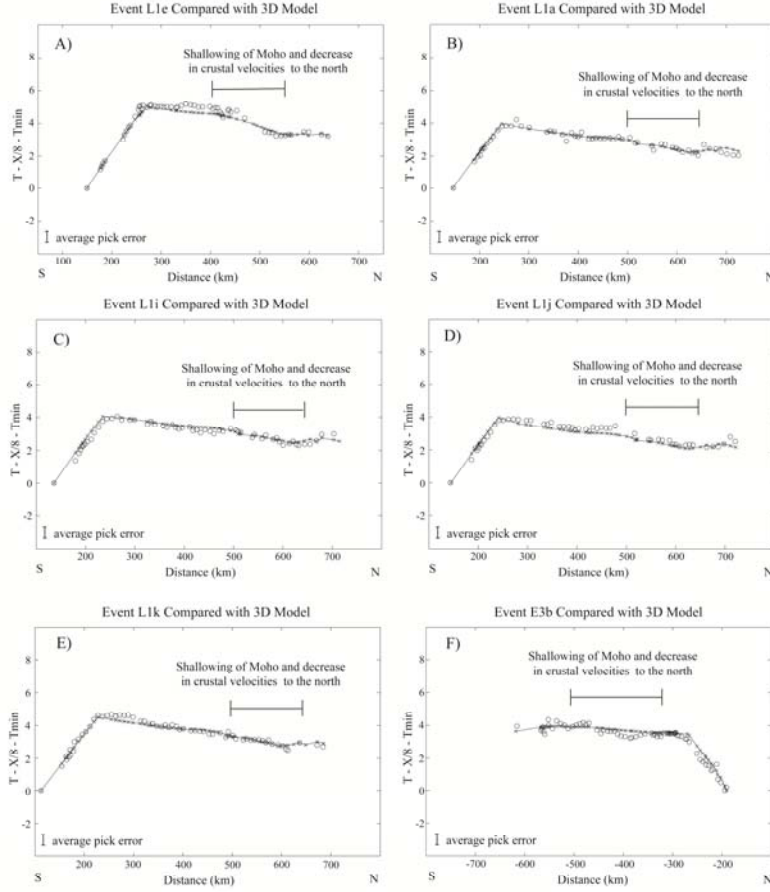


Figure 4. These plots show observed P-wave travel times (circles) and calculated travel times (lines and crosses) for the far-regional events, (A) L1e, (B) L1a, (C) L1i, (D) L1j, (E) L1k, and (F) E3b. The horizontal bars highlight the locations of the transition for shallowing of the Moho.

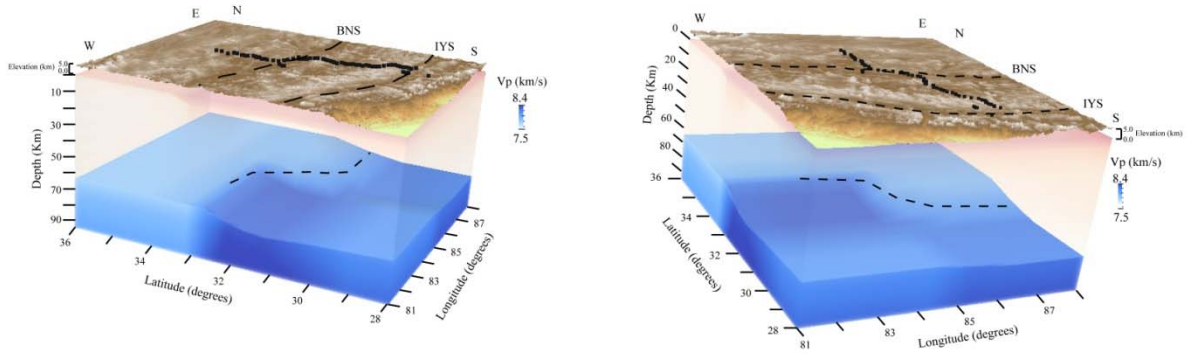


Figure 5. The 3D Moho and upper-mantle velocity structure found in this study for the region of the Hi-CLIMB array, with the left plot showing a view from the west and the right plot showing a view from the south.

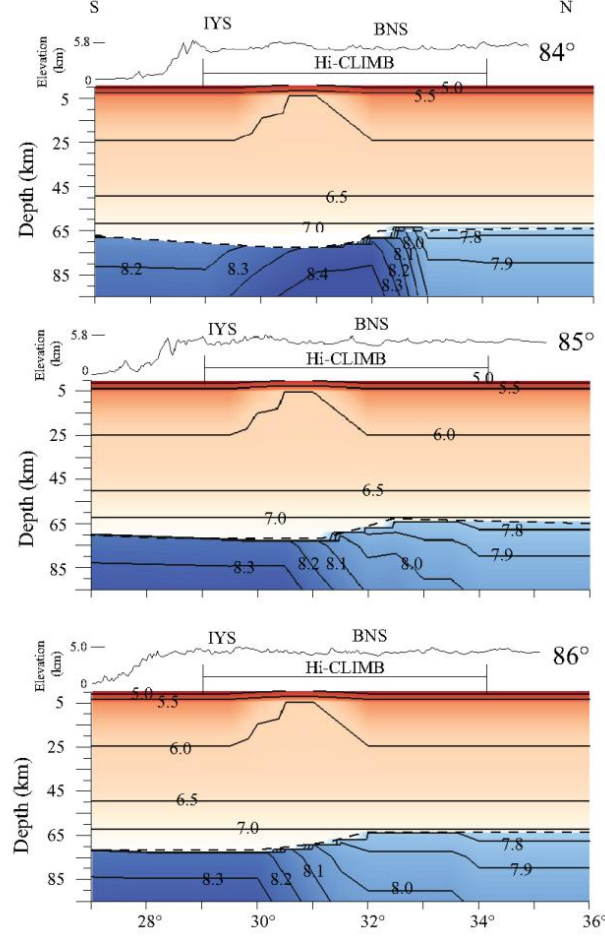


Figure 6. North-south cross-sections of the 3D velocity model of Griffin et al. (2011) along longitudes of 84, 85 and 86 degrees.

4. SPECTRAL ELEMENT MODELING OF THE P_n PHASE

The P_n phase is typically not a simple head wave but is composed of a complex set of interfering waves when there is a positive velocity gradient with respect to depth below the Moho interface (Cerveny and Ravindra, 1971; Hill, 1971; Menke and Richards, 1980). These interfering waves can also simply result from the spherical nature of the Earth (Hill, 1973; Sereno and Given, 1990; Yang et al., 2007), which gives an effect equivalent to a velocity gradient in a corresponding flattened Earth model. How observed amplitudes of refracted waves change over distance supports the interpretation that these arrivals are composed of diving and interference waves and is in contrast to a pure head wave (Braile and Smith, 1975). To account for the intricate nature of P_n propagation, we have implemented the spectral element method (SEM) (Komatitsch and Vilotte, 1998; Komatitsch et al., 2005). SEM can be applied in 2D or 3D and implemented in parallel using message passing interface (MPI) on large-cluster computing. Here we have applied a 2D viscoelastic SEM code. For validity tests of the SEM applied to the P_n phase, see Appendix B. As a practical measure, essential features of P_n waveforms are distilled into seismic attributes, including arrival times, envelopes of

wave amplitudes, and pulse frequencies for modeling using the approach of Matheney and Nowack (1995) (see Appendix A).

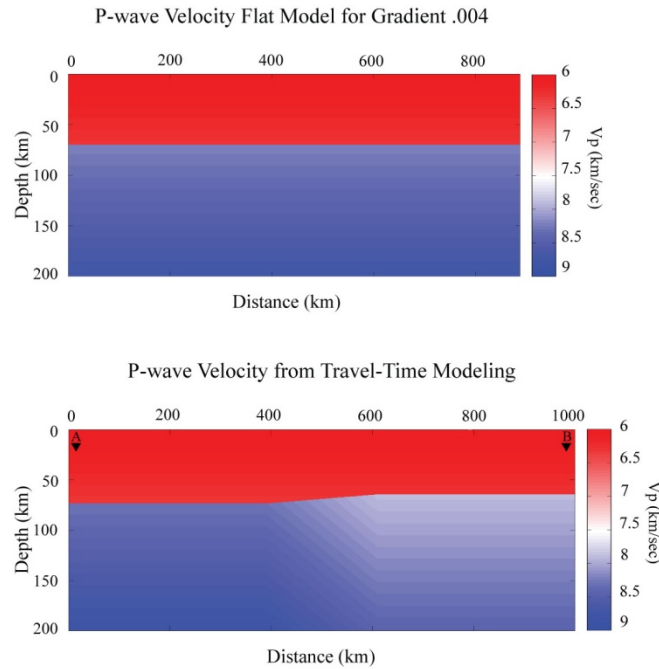


Figure 7. The top plot shows the P-wave velocities for a simple layer over a gradient with an upper-mantle velocity gradient of .004 1/s. The bottom plot shows a simplified P-wave velocity model from travel-time modeling of regional events from Hi-CLIMB, showing a step in the Moho.

To test the effects of upper-mantle velocity gradient, Moho topography, and lateral velocity variation on P_n propagation, we designed two velocity models. The top plot of Figure 7 shows the P-wave velocity model for a laterally homogeneous flat model with an upper-mantle velocity gradient of .004 1/s and has a crustal layer above a half space, with the Moho at 70 km depth. The bottom plot of Figure 7 shows a simplified 2D slice of a model derived from the 3D travel-time modeling, using regional data from the Hi-CLIMB array. Both the crust and the upper mantle have velocity gradients with depth and velocities that change laterally. The Moho changes in depth from 73.4 km on the left side of the model to 64.3 km on the right side of the model.

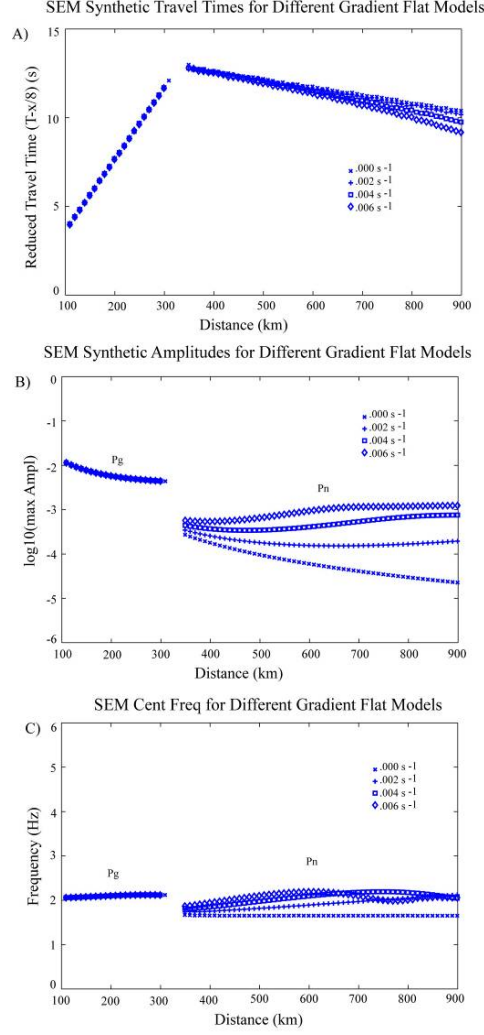


Figure 8. SEM synthetic P-wave A) travel-times, B) amplitudes and C) pulse centroid frequencies for a flat Moho with several velocity models with different upper-mantle velocity gradients of 0.0, 0.002, 0.004, and 0.006 1/s. For this case no Q is included.

Figure 8 shows the first arrival amplitudes for several laterally homogeneous models with different upper-mantle velocity gradients of 0, 0.002, 0.004, and 0.006 1/s. The incident pulse is a Ricker wavelet with a center frequency of 2 Hz and filtered from .5 to 2.5 Hz. The case where the upper-mantle gradient is .004 1/s is the model shown in Figure 7 (upper plot). As seen in Figure 8, when there is no upper mantle velocity gradient, the P_n pulse amplitudes decrease with distance from 300 to 800 km. For the existence of an upper mantle gradient, the travel-time curves now curve, but the effect is the most pronounced for the highest gradients. For an upper-mantle velocity gradient greater than .004, the P_n pulse amplitudes increase for this distance range. The pulse centroid frequencies go down at the intersection of the Pg and P_n branches, but then recover and even oscillate with distance for the highest upper mantle velocity gradients.

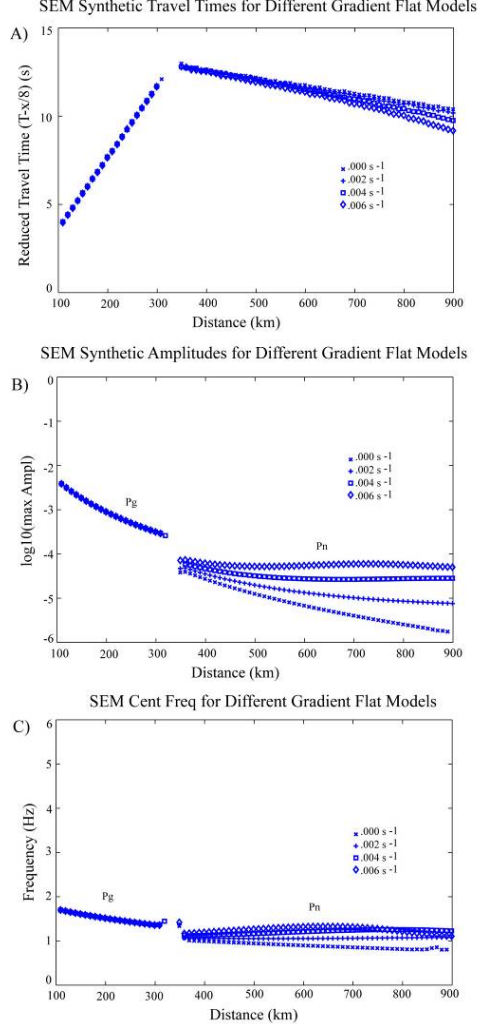


Figure 9. SEM synthetic P-wave A) travel-times, B) amplitudes and C) pulse centroid frequencies for a flat Moho with several velocity models with different upper-mantle velocity gradients of 0.0, 0.002, 0.004, and 0.006 1/s. For this case a Q of 150 is assumed in the crust and 400 in the mantle.

In Figure 9, a similar case as in Figure 8 is shown with a Q of 150 in the crust and 400 in the mantle. The travel-times are the same as before and still bend down for increasing upper mantle velocity gradient. However, the attenuation has the effect of bringing down all the amplitude curves. None theless, the amplitude pattern is still preserved. The pulse centroid frequencies are also brought down.

Figure 10 shows the travel-times, amplitudes and pulse centroid frequencies computed for the velocity model shown in the lower plot of Figure 7, with a step in the Moho. The crosses are for source B near 1000 km and recorded to the south in Figure 7 (right plot), and the circles are for source A near 0 km and recorded to the north in Figure 7 (right plot). The travel-time curves are quite distinct between the reversed events resulting from the different upper mantle top velocities to the left and right of the model, as well as the change of Moho structure across the model. The amplitudes curves in

Figure 10 show a relative increase with distance for the Pn branch for source B, resulting from the step in the Moho for this particular upper-mantle velocity gradient. However, for source A, the Pn amplitudes relatively decrease with distance, resulting from the step in the Moho. However, the effects of the Moho step on the pulse frequencies are less dramatic. In any case, using events at different locations to the north and south of the Hi-CLIMB array, one can identify the large-scale structural features.

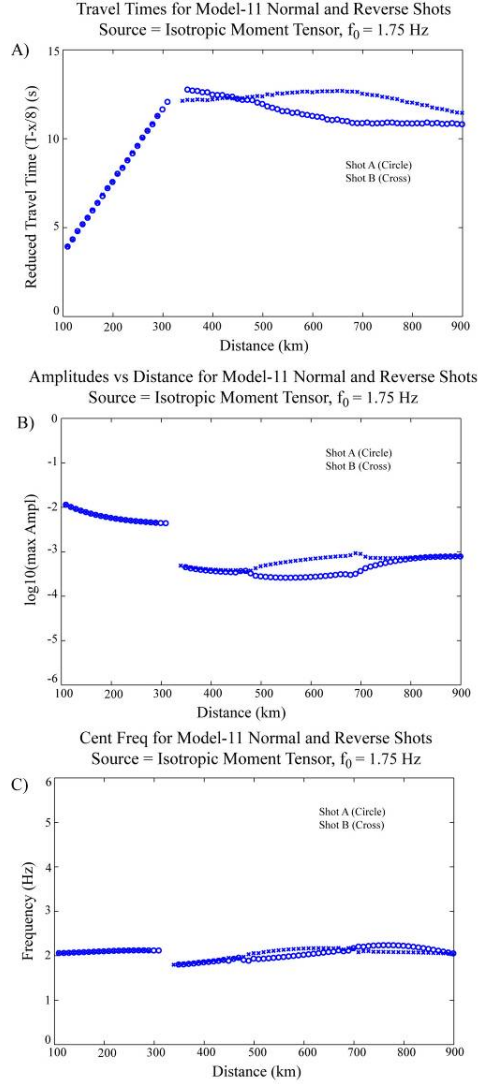


Figure 10. SEM synthetic A) travel-times, B) amplitudes and C) pulse centroid frequencies for a step in the Moho, as shown for the right plot in Figure 7. The crosses for source B near 1000 km in Figure 7 (right plot) and recorded to the south, and the circles are for a source A near 0 km and recorded to the north in Figure 7 (right plot).

Figure 11 shows the case of a step in the Moho given in the right plot in Figure 7, only now with attenuation included. The crust now has a Q of 150 and the upper mantle has a Q of 400. Once again the travel-times are the same as the no attenuation case shown

in Figure 10. For the attenuation case in Figure 11, the amplitudes are brought down but with a similar pattern as in the no attenuation case. Also, the effect of the step in the Moho on pulse frequencies is more subdued in the case with attenuation. However, the Pn pulse frequencies still show a slight increase with frequencies resulting from the upper mantle velocity gradient.

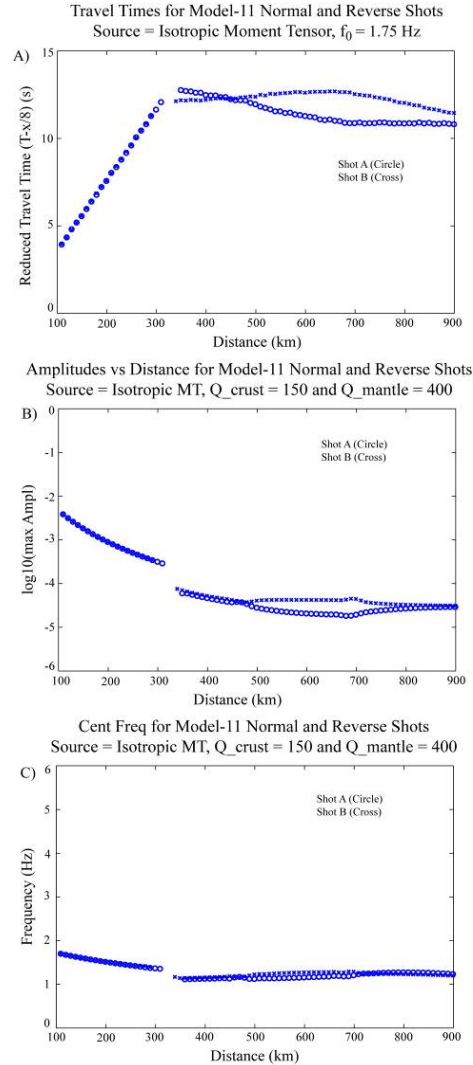


Figure 11. SEM synthetic A) travel-times, B) amplitudes and C) pulse centroid frequencies for a step in the Moho, as shown for the right plot in Figure 7. The crosses for source B near 1000 km in Figure 7 (right plot) and recorded to the south, and the circles are for a source A near 0 km and recorded to the north in Figure 7 (right plot).

5. MOMENT TENSORS OF REGIONAL EVENTS IN TIBET

We have compiled the centroid moment tensor solutions of regional earthquakes that are relevant to those selected for constructing Pn profiles from CMT focal

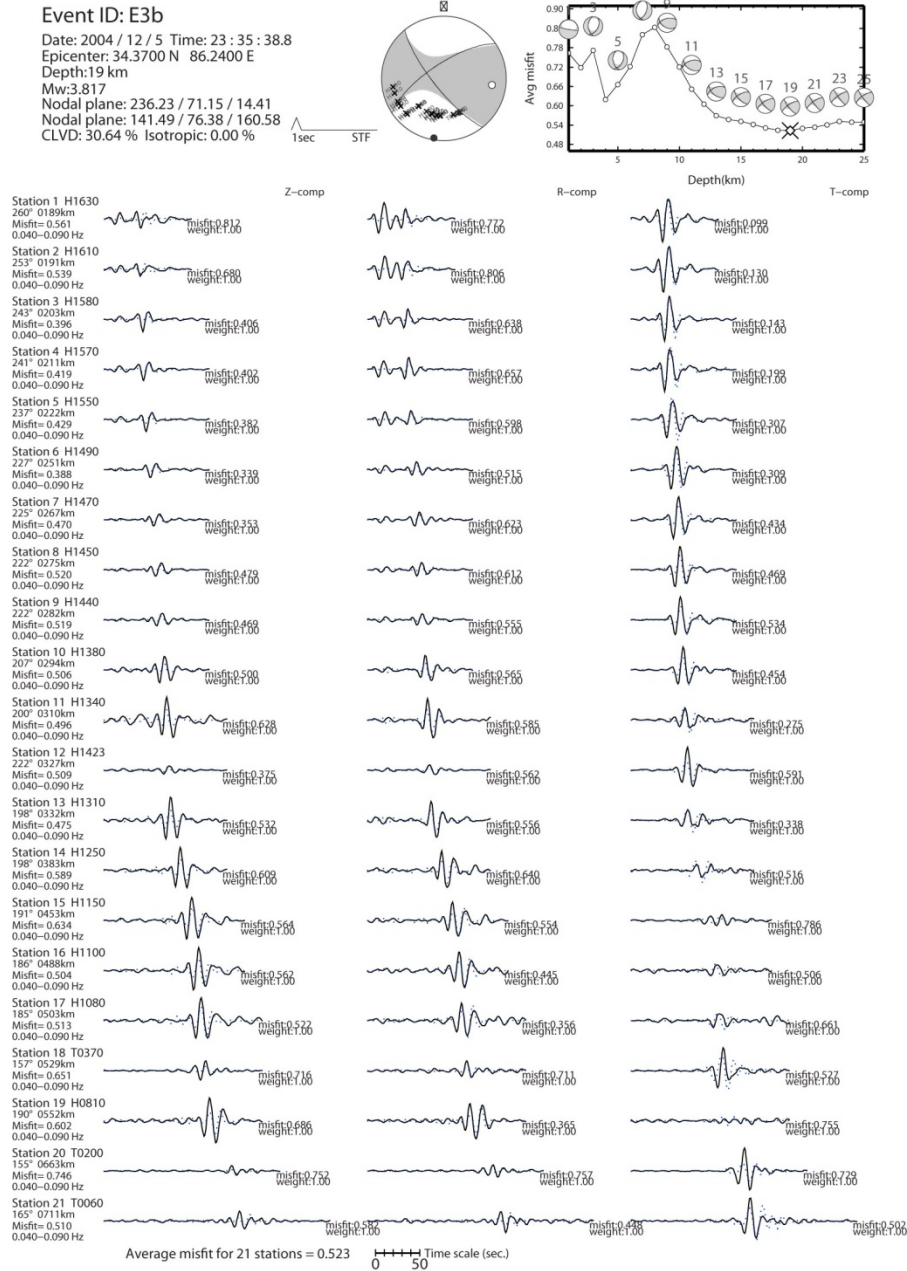


Figure 12. Inversion of three-component waveforms for the focal-mechanism of event E3b using data from the Hi-CLIMB array. The top right plot shows the data misfit with a narrow minimum at 6 km and a broad flat minimum at 19 km, and the upper left plot shows the 19 km solution. The lower plots show the matches between the observed and calculated waveform data.

mechanisms of Dziewonski et al. (1981) and from Baur (2007). However, event E3b and some of the smaller events did not have previously derived focal mechanisms. For the Hi-CLIMB array-station geometry for some of the regional events, making a determination of the focal mechanisms is relatively challenging even though the data waveform quality is very high from the Hi-CLIMB array. As such, Tai-Lin Tseng of our group checked

with the regional LSA station (the only permanent regional seismic station) and other temporary arrays in Tibet for their availability and tried to include them in the moment tensor inversions. She found that for a number of earthquakes investigated they are either shallow normal faults on the rifts or strike-slip faults occurring in the upper crust. However, both types of mechanisms show generally E-W extensional stresses which are typical for the Tibet area.

As an example of a focal mechanism inversion, Figure 12 shows the determination of the focal mechanism for event E3b using seismic waveform data recorded by the Hi-CLIMB array. The top right plot shows the data misfit with a narrow minimum at 5 km and a broad flat minimum at 19 km. Figure 12 also shows the waveform matches between the observed and calculated long period data for the 19 km solution. For this event, the seismograms for the permanent seismic station LSA were poor.

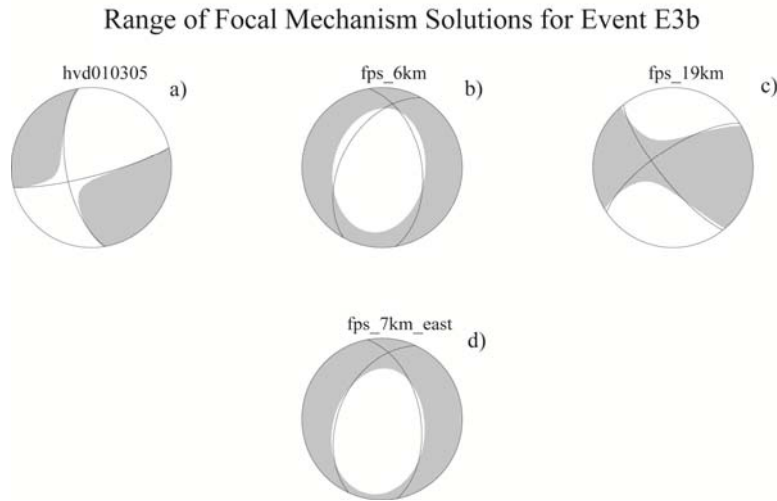


Figure 13. Focal mechanism solutions for Event E3b. a) A comparison global CMT focal mechanism for an earthquake located about 70 km distant from Event E3b. b) The focal mechanism solution for Event E3b with a data misfit minimum at a depth of 6 km. c) The focal mechanism solution for Event E3b with a data misfit minimum at a depth of 19 km. d) The focal mechanism for Event E3b for a shift in epicenter of 10 km to the east resulting in a least misfit minimum at the shallower depth of 7 km. All solutions indicate East-West extension.

Figure 13 shows a summary of the focal mechanism solutions for Event E3b. As a comparison, Fig. 13a shows a global CMT focal mechanism of an earthquake located about 70 km distant from Event E3b. For E3b, there are two local minimum, one narrow at around 6 km in depth (Fig. 13b), and one broad and flat at around 19 km depth (Fig. 13c). However, the average misfits for this event are still relatively large at any depth, and both solutions have high CLVD components. This initially suggested to us that there could be either variations in the local velocity model or event location issues that could need to be accounted for.

An additional experiment was done to check the sensitivity to the epicentral location and the moment tensor solutions were mostly stable, except for a epicentral shift of about 10 km to the east which resulted in the shallow solution at 7 km becoming the solution with the smallest data misfit (Fig. 13d), and is similar to the earlier misfit minimum solution at 6 km. Nonetheless, Event E3b has a large azimuthal gap making it a challenging event to get a reliable focal mechanism solution for. However all solutions for this event indicate overall east-west extension. We are currently using both inverted mechanisms for event E3b for the modeling of *Pn* seismic attributes.

6. SPECIFICATION OF THE MOMENT TENSOR FOR 2D SEM MODELING

For the specification of the moment tensor in the 2D SEM modeling, we first tested several 2D azimuth slices of a 3D moment tensor along specific azimuths for a particular double-couple moment tensor (left plot of the figure 14). The *Pg* and *Pn* take-off angles

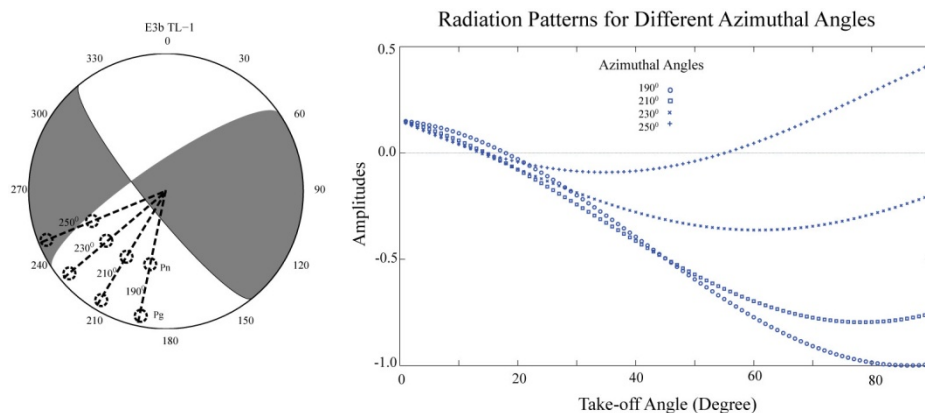


Figure 14. The left plot shows the 3D focal mechanism for a particular double-couple moment tensor source with four angles given by dashed lines. The *Pg* and *Pn* take-off angles are shown by small circles. The right plot shows the amplitudes on the focal sphere of the 2D moment tensor for the azimuthal angles given in the left plot as a function of take-off angle derived from the 3D moment tensor.

are shown by small circles. The radiation pattern terms resulting from implementing a rotated 2D moment tensor derived from the 3D moment tensor are then shown in the right plot of figure 14.

We next compare the P-wave amplitudes with the amplitudes from the 2D Specfem2D code using the rotated 2D moment tensor formulas. Based on these tests, we inferred that an additional 180° azimuthal rotation is needed to match the amplitudes of the rotated moment tensor. With this modification, the *Pn* and *Pg* amplitude computed from the SEM code are shown in figure 15 for the focal mechanisms given the plot to the left using four azimuthal angles.

7. MODELING PN SEISMIC ATTRIBUTES IN TIBET

Numerical modeling of Pn wave attributes, including the travel-times, the peak envelope amplitudes, and the instantaneous pulse frequencies, was performed for six

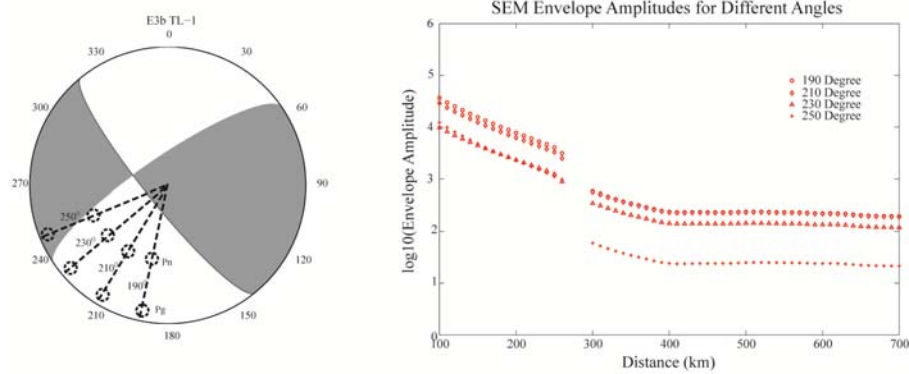


Figure 15. The left plot shows a focal mechanism with four azimuthal angles given by dashed lines. The Pn and Pg take-off angles are shown by the small circles. The right plot shows the SEM envelope amplitudes for the azimuthal angles given on the left. Different symbols represent different azimuthal angles.

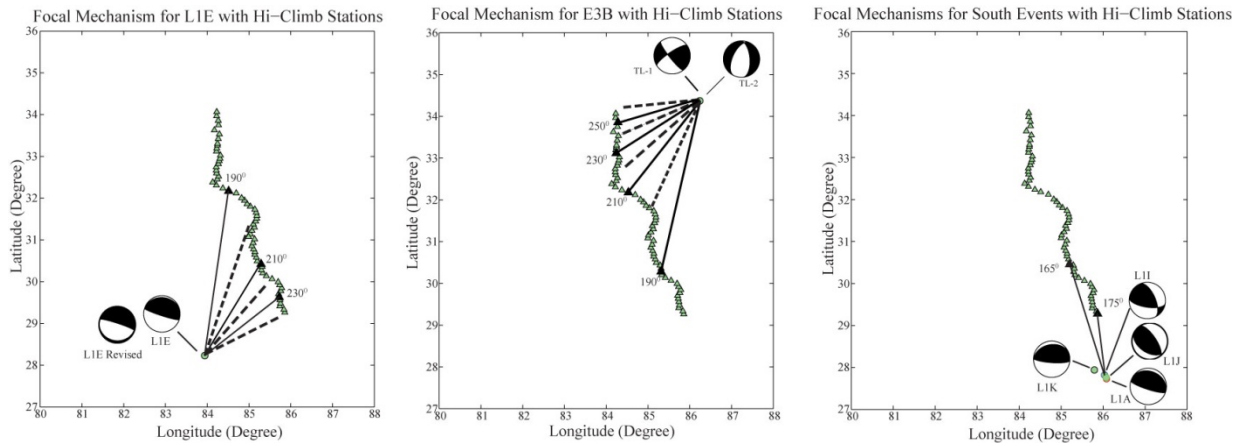


Figure 16. The left map shows the original and slightly revised focal mechanism for event L1E. The middle map shows the focal mechanism TL-1 and an alternative focal mechanism TL-2 for event E3B. The right map shows the focal mechanisms for the cluster of south events L1A, L1I, L1J, and L1K. The triangles show the Hi-Climb stations, where the solid triangles along with the solid lines show the orientation angles used for the specification of the moment tensor. The dashed lines show the separation of ranges used to specify the moment tensor.

regional earthquakes recorded by the Hi-Climb array in Tibet. Earthquakes are chosen to be approximately in-line with the Hi-Climb array, but also include both P_g and P_n arrivals along with the cross-over distance. The location of the events used here are shown in figure 16.

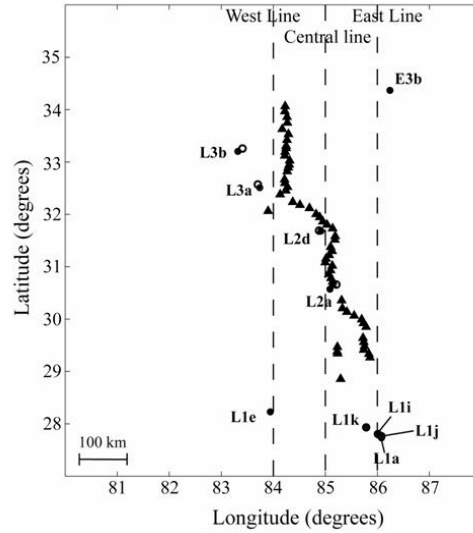


Figure 17. This map shows the locations where 2D P-wave velocity slices were obtained from the 3D velocity model of Griffin et al. (2011). Triangles represent the Hi-Climb array. The circles show the events used by Griffin et al. (2011) for the 3D velocity model where the open circles are relocations. The dashed lines show the West, Central, and East lines for the 2D slices.

For the SEM synthetic calculations using the selected Hi-Climb events, P-wave velocities, upper mantle velocity gradients, and the Moho structures from Griffin et al. (2011) was used. The Moho structure found by Griffin et al. (2011) using regional travel-times is similar to that found by Tseng et al. (2009) and Nowack et al. (2010) using teleseismic waves. The upper mantle top velocities and velocity gradients from Griffin et al. (2011) are similar to those found by Phillips et al. (2007). These are also similar to those found by Myers et al. (2010) in the southern Lhasa terrane, but the velocity gradients from Myers et al. (2010) are lower in the northern Qiangtang terrane.

Griffin et al. (2011) used the 3D ray tracing code CRT of Cervený et al. (1988) for modeling the travel-times and imaged a 3D P-wave velocity model along with the Moho structure. From this 3D model, 2D slices were obtained for use in the 2D spectral-element method (SEM) modeling. The location of the 2D slices and the 3D P-wave velocity model of Griffin et al. (2011) are given in figure 17. On the 2D slice along the longitude of 84° (West Line) is considered for the south event L1E for the seismic attribute modeling. Another 2D slice along the longitude of 85° (Central Line) is considered for the south cluster of events L1A, L1I, L1J, and L1K. The 2D slice along the longitude of 86° (East Line) is considered for the north event E3B. Figure 18 shows the P-wave velocity slices for the event L1E, the event E3B, and the cluster of events

L1A, L1I, L1J, and L1K. These velocity profiles are then earth flattened for input into the SEM code (see Bakir, 2011).

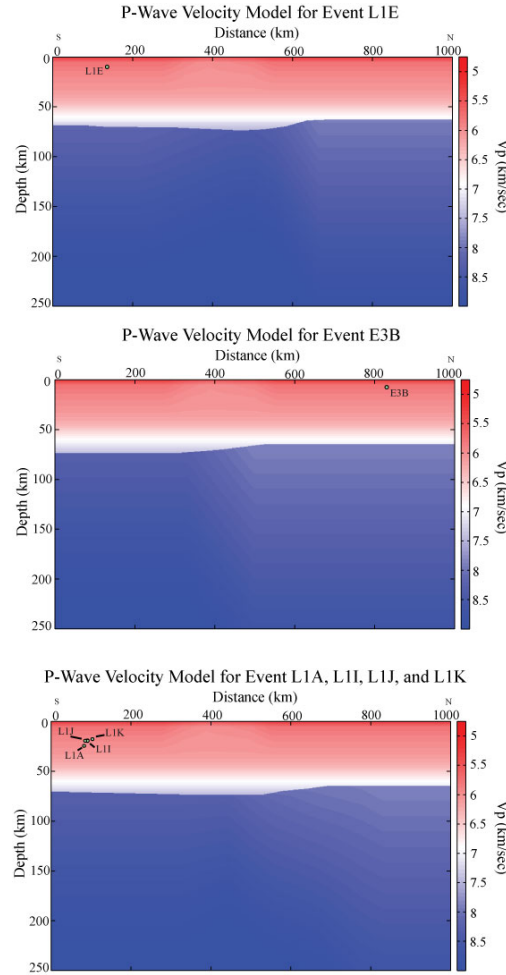


Figure 18. The plots show the P-velocities for 3 different slices of the 3D model of Griffin et al. (2011) which have constant upper mantle velocity gradients but different upper mantle top velocities. The small circles show the locations of the events used with each velocity slice.

The moment tensor solutions of the far regional 6 events were obtained from Baur (2007) for all events except E3B which was obtained from Tai-Lin Tseng from our group and described earlier. For the numerical calculations, SPECFEM2D, a parallel SEM code (Komatitsch and Vilotte, 1998 and Komatitsch et al., 2005), was used similar to the previous numerical tests. For each event, multiple 2D moment tensor sources are calculated for different azimuth angles from the events to the Hi-C limb stations. Two, three, or four stations are selected for the orientation of the moment tensor depending on how much the focal mechanism solutions are affected by the azimuth to the stations. Three stations are chosen for L1E for the specification of the moment tensor. Four stations are chosen for E3B since it is the most out-of-line event and stations get closer to the nodal planes for the different azimuth angles. Two stations are found to be sufficient

for the cluster of events L1A, L1I, L1J, and L1K since they are the most in-line with the Hi-CLIMB array.

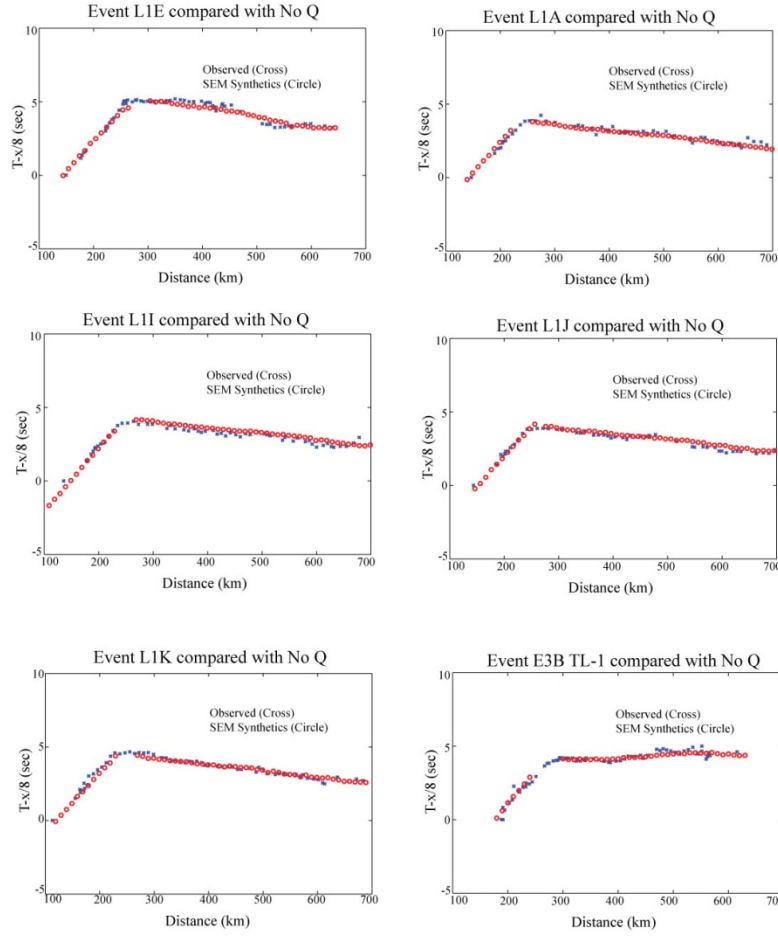


Figure 19. These plots show the calculated travel-times of the selected events with no attenuation in the SEM models compared with the observed travel-times. Circles are the SEM calculated travel-times and crosses are observed travel-times.

In all peak envelope amplitude and pulse frequency figures, vertical dashed lines are used to represent different distance ranges defined by the different orientation angles used for the 2D moment tensors. The approximate orientation angles and the strike, rake, and dip of the events are used to calculate the moment tensor entries of the focal mechanisms. Once, a rotated 3D moment tensor matrix is obtained as described by Bakir (2011), only the x and z components of the rotated moment tensor are input into the 2D SEM calculations. Figure 16 shows the moment tensors of the selected events, the Hi-CLIMB array, and the orientation angles from the events to the selected stations on a regional map for the specification of the 2D moment tensors.

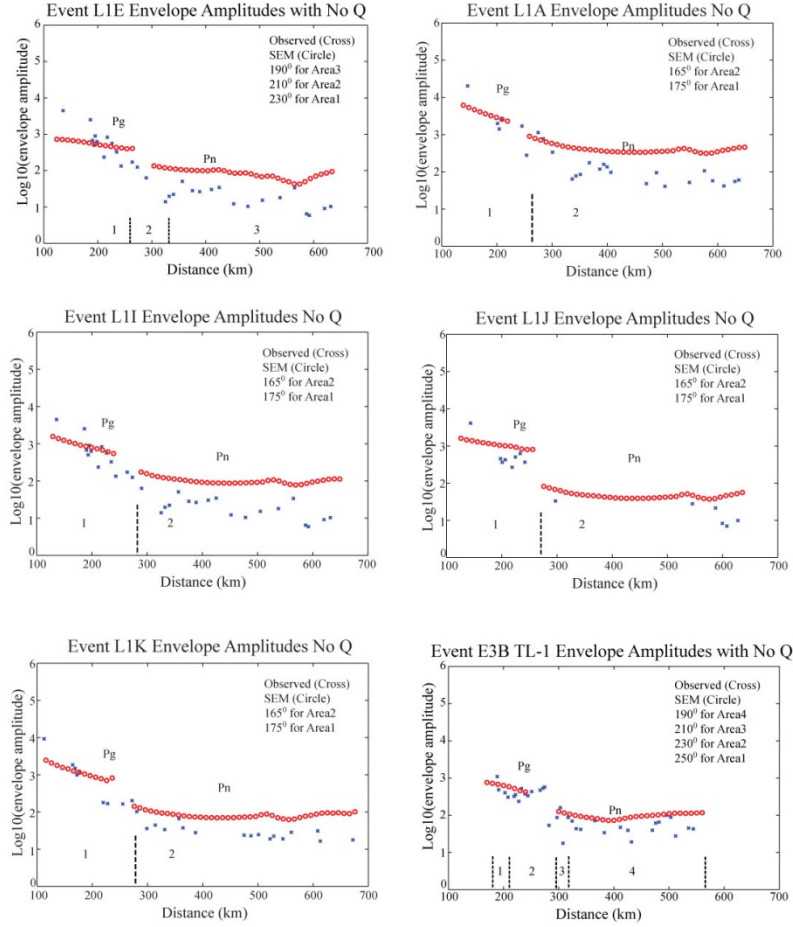


Figure 20. These plots show the peak envelope amplitudes of the selected events with no attenuation in the SEM models compared with the observed envelope amplitudes. The circles are the SEM calculated values and the crosses are observed envelope amplitudes. The distance ranges for the specified orientation angles for the moment tensor are also shown. For event L1E, the modified moment tensor is used and for event E3B the TL-1 moment tensor is shown.

Travel-times from the SEM elastic calculations are first matched with the observed travel-times from regional earthquakes recorded by the Hi-CLIMB array in figure 19. From figure 19, it can be seen that the 2D slices derived from the 3D model of Griffin et al. (2011) do a reasonable job of matching the observed travel-times. The peak envelope amplitudes and the pulse frequencies of the SEM calculations are then compared with the observed data. Because the SEM results will be compared with the observed data, the 2D SEM amplitudes are corrected for out-of-plane spreading (see Bakir, 2011). Both the centroid pulse frequencies and the instantaneous frequencies are used to describe the frequency characteristics of the data using the approach described by Matheny and Nowack (1995).

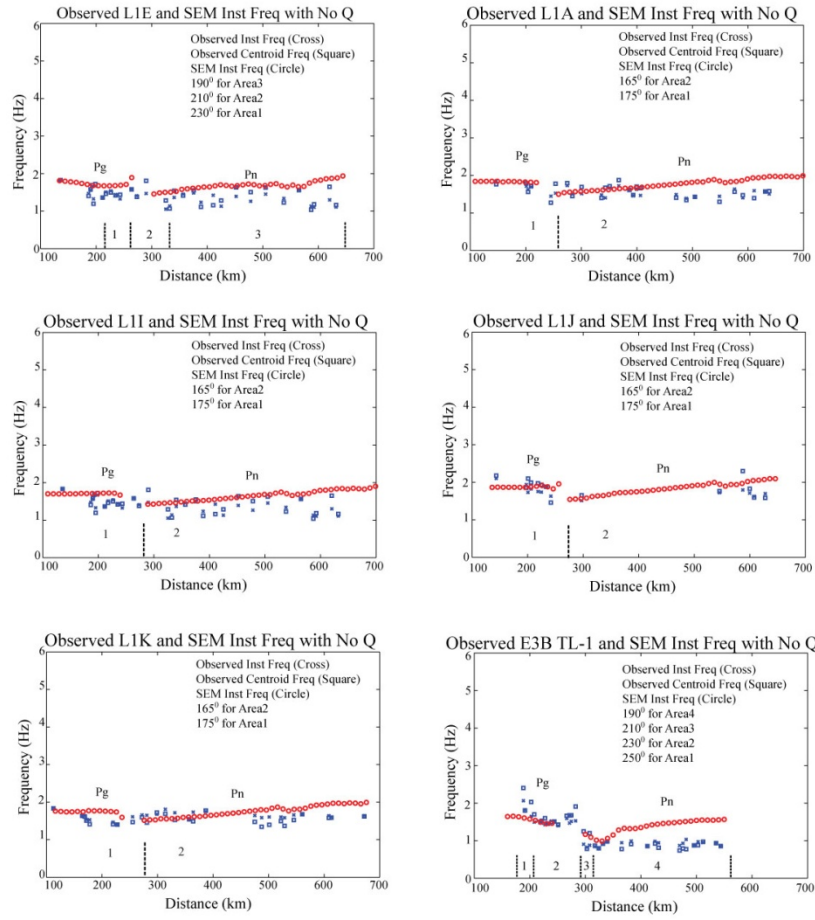


Figure 21. These plot show the calculated instantaneous pulse frequencies of the selected events with no attenuation for the SEM models compared with the observed instantaneous and pulse frequencies. The circles are the SEM calculations and the crosses and squares are the observed instantaneous and centroid frequencies. For event L1E, the modified moment tensor is used and for event E3B the TL-1 moment tensor is shown.

Figure 20 shows the calculated peak envelope amplitudes of the elastic SEM calculations assuming no attenuation compared with the observed peak envelope amplitudes for the six events. For event L1E, the revised moment tensor is used to avoid small amplitudes of the P_g branch being too close the nodal plane for the original moment tensor of Baur (2007). However, this was within the error of the determination of the moment tensor (J. Nabelek, personal communication). For event E3B, there were two allowed focal mechanisms as derived by Tai- Lin Tseng. Here, we give the results for focal mechanism TL-1 shown in Figure 16. However, the results for TL-2 were similar and are given by Bakir (2011).

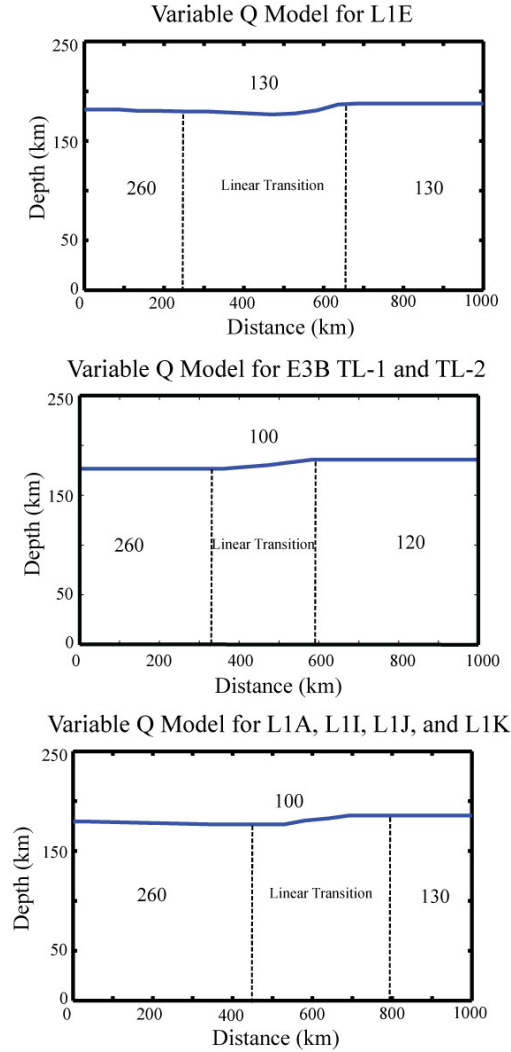


Figure 22. These plots show variable upper mantle Q models for each slice determined from modeling seismic attributes from the selected regional events assuming the velocity slices in Figure 18.

Figure 21 shows the pulse frequencies using the elastic SEM calculations with no attenuation compared with the observed instantaneous pulse frequencies. The calculated pulse frequencies for the Pn branch increase with distance resulting from the upper mantle velocity gradient obtained from the 3D models Griffin et al. (2011) and similar to those obtained by Phillips et al. (2007). The pulse frequencies can be reduced by either increasing the attenuation or lowering the velocity gradient in the upper mantle. However, both the calculated envelope amplitudes and pulse frequencies are too high when using no attenuation for these models compared to the observed data. From this we conclude that attenuation or a lower gradient in the upper mantle is needed to match the amplitudes and pulse frequencies with the observed attributes.

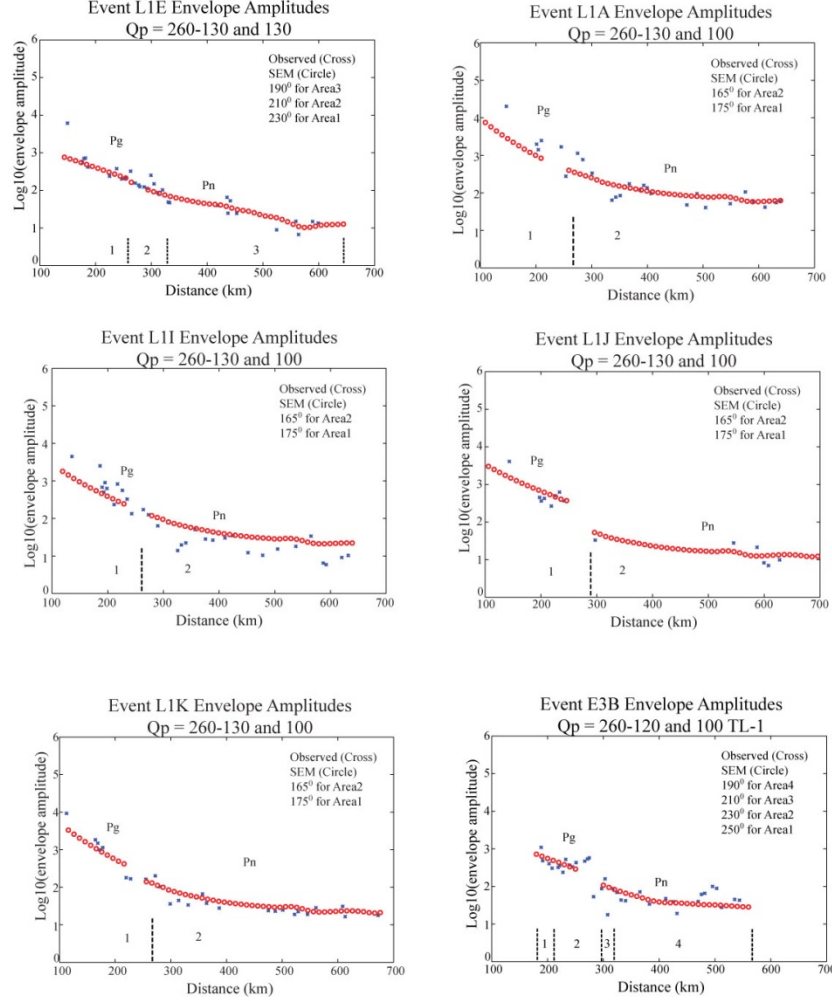


Figure 23. These plots show the SEM calculated peak envelope amplitudes of the selected events with the attenuation models shown in Figure 22 and the velocity slices given in Figure 18 compared with the observed envelope amplitudes. The circles are the SEM calculated values and the crosses are observed envelope amplitudes. The distance ranges for the specified orientation angles for the moment tensor are also shown. For event L1E, the modified moment tensor is used and for event E3B the TL-1 moment tensor is shown.

From the modeling of the amplitudes and pulse frequencies given in figures 20, and 21, this suggests that upper mantle attenuation is appropriate to apply for all the events. For the modeling here, we first use the structural models obtained from Griffin et al. (2011) and then include seismic attenuation. A constant Q attenuation with frequency is provided in the spectral element code, and given that the data and the synthetics are both filtered in the band between .5 to 2.5 Hz is probably appropriate. However, further tests of this will be required in the future.

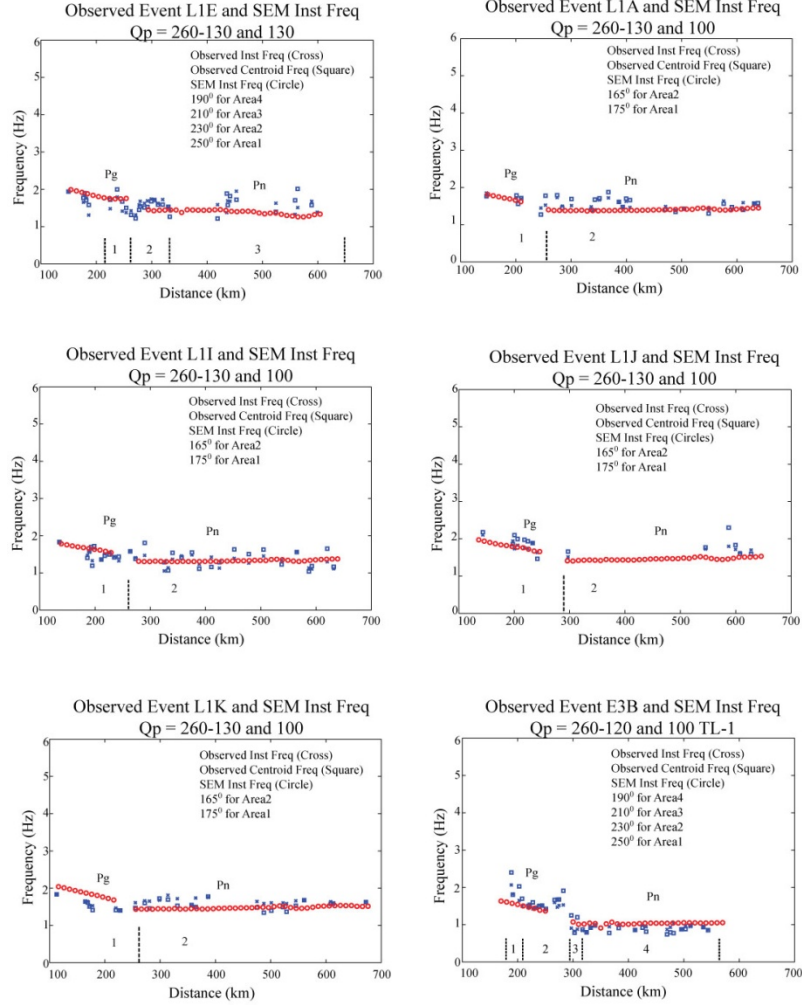


Figure 24. These plots show the SEM calculated pulse frequencies of the selected events with the attenuation models shown in Figure 22 and the velocity slices given in Figure 18 compared with the observed pulse frequencies. The circles are the SEM calculations and the crosses and squares are the observed instantaneous and centroid frequencies. For event L1E, the modified moment tensor is used and for event E3B the TL-1 moment tensor is shown.

For the southwest event L1E, a Qp of 130 in the crust, a Qp of 260 in the Lhasa terrane to the south and a Qp of 130 in the Qiangtang terrane in the north for the upper mantle was used for the SEM modeling. For the south cluster events, Qp values were inferred to be the same as event L1E, except a Qp of 100 is used in the crust. For the north event E3B, a Qp of 100 in the crust and a Qp of 260 for the Lhasa terrane in the south and a Qp of 120 for the Qiangtang terrane in the north was used in the upper mantle. When a variable Qp exists, a smooth transition is created around the ramp structure of the Moho for the SEM models. The variable Qp models of these events are shown in figure 22.

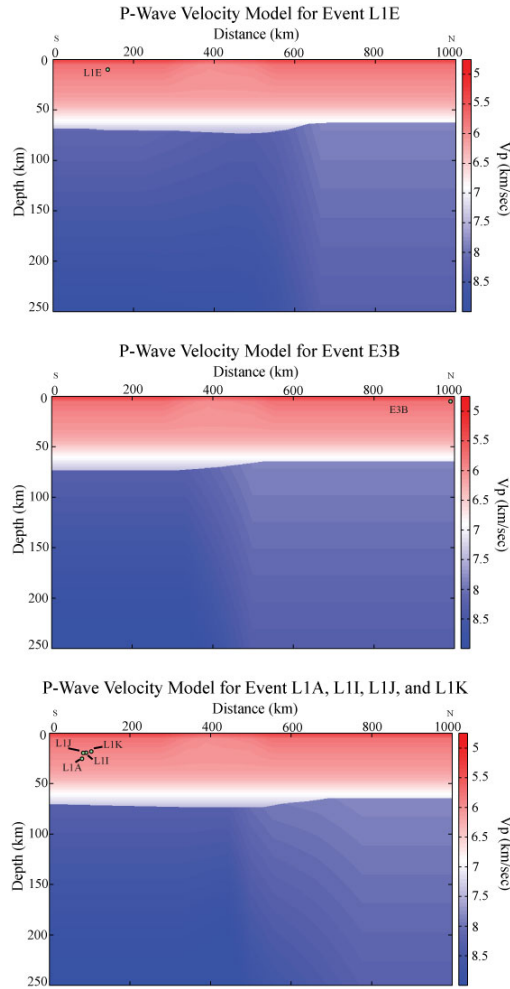


Figure 25. The plots show the P-velocities for 3 different slices of the 3D model of Griffin et al. (2011) which variable upper mantle velocity gradients. The small circles show location of the events used with each velocity slice.

In figure 23, the SEM envelope amplitude with variable attenuation and a constant velocity gradient in the upper mantle are compared with the observed peak envelope amplitudes and in figure 24 the computed pulse frequencies are compared with the observed instantaneous and centroid frequencies. From figures 23 and 24, it is observed that the SEM modeling with variable attenuation and a constant upper mantle velocity gradient gives a better fit to the seismic attributes than the earlier case with no attenuation.

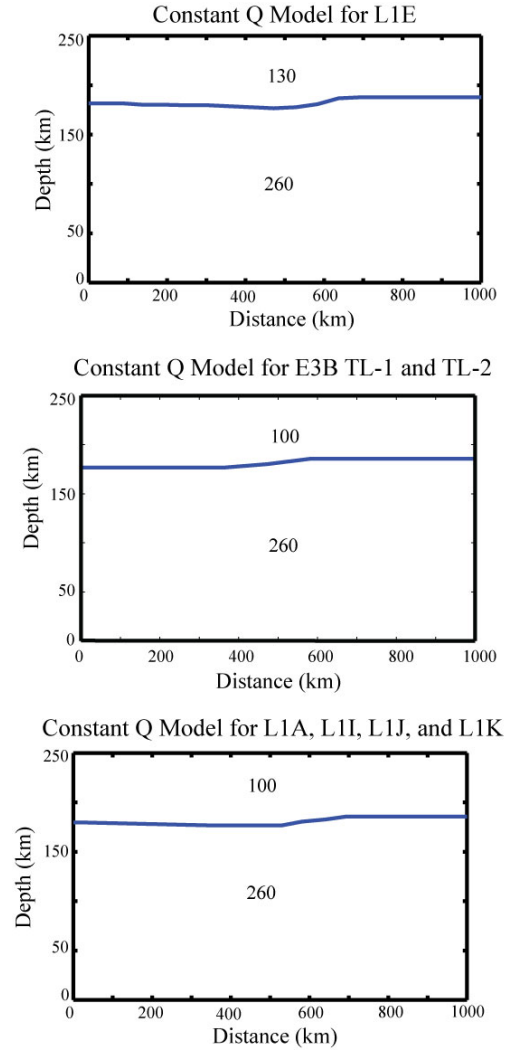


Figure 26. The plots shows constant upper mantle attenuation used with the velocity models in Figure 25 with a laterally variable upper mantle velocity gradient between the Lhasa and Qiangtang terranes.

We next investigate if velocity models with variable upper mantle velocity gradients can give similar results for the modeling of seismic attributes for the distance ranges used here. A variable upper mantle gradient structure is constructed for all the 2D slices and input into the SEM calculations. A constant Q_p of 260 is chosen for the entire upper mantle along with a variable upper mantle velocity gradient. Figure 25 shows the variable gradient P-wave velocity slices for the southeast event L1E, the north event E3B, and for the south cluster events L1A, L1I, L1J, and L1K. While the earlier P-wave velocity slices had a velocity gradient of 0.003 sec^{-1} over the entire upper mantle before the earth-flattening, the variable velocity gradient slices have a velocity gradient of 0.003 sec^{-1} in the Lhasa terrane to the south and a velocity gradient of 0.001 sec^{-1} in the

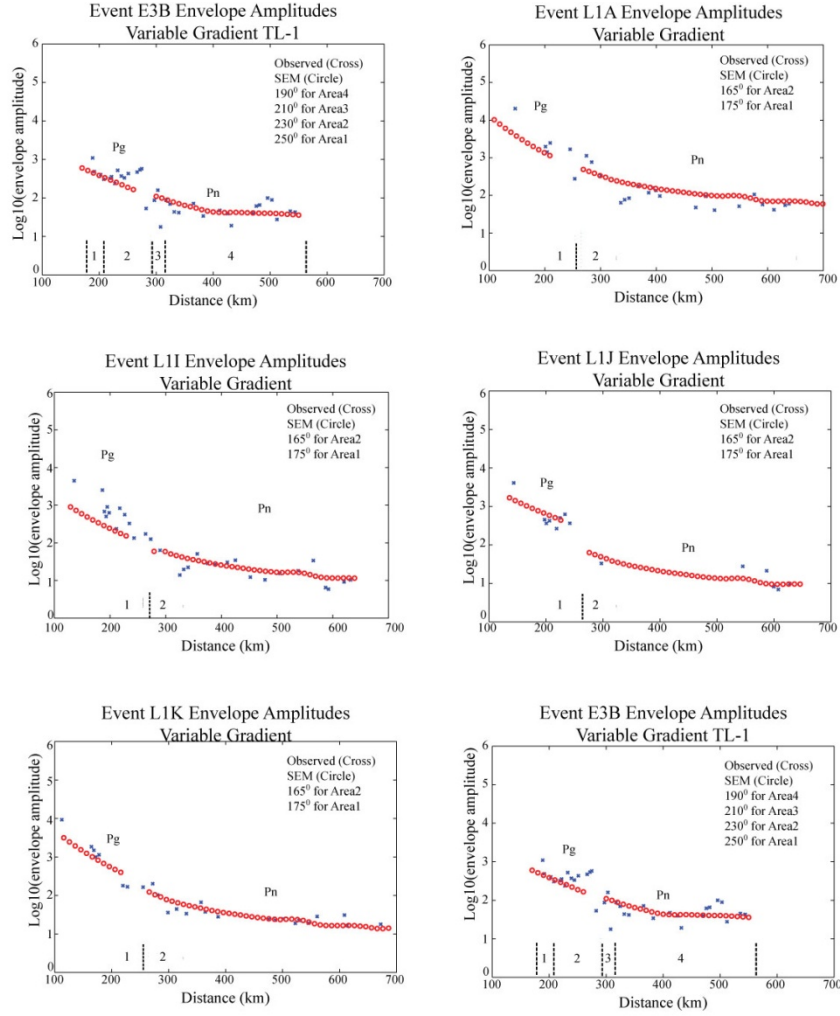


Figure 27. These plots show the peak envelope amplitudes of the selected events with a constant attenuation in the upper mantle for the SEM models compared with the observed envelope amplitudes. The circles are the SEM calculations and the crosses are observe envelope amplitudes.

Qiangtang terrane to the north. This is similar to the upper mantle velocity gradient model of Myers et al. (2010) for this region. The corresponding Q models with constant upper mantle attenuation are shown in figure 26.

For all events, the viscoelastic SEM results with constant attenuation and a variable upper mantle gradient structure are then compared with the observed data. In figure 27, a comparison of the SEM amplitudes with constant attenuation and a variable upper mantle gradient with the observed amplitudes is given, and in figure 28 a comparison of the SEM pulse frequencies with the observed instantaneous and centroid pulse frequencies is shown. The modeling results are similar to the results obtained for the variable attenuation and constant gradient results. This suggests a trade-off in model parameters between upper mantle attenuation and upper mantle velocity gradients using the amplitude and pulse frequency data.

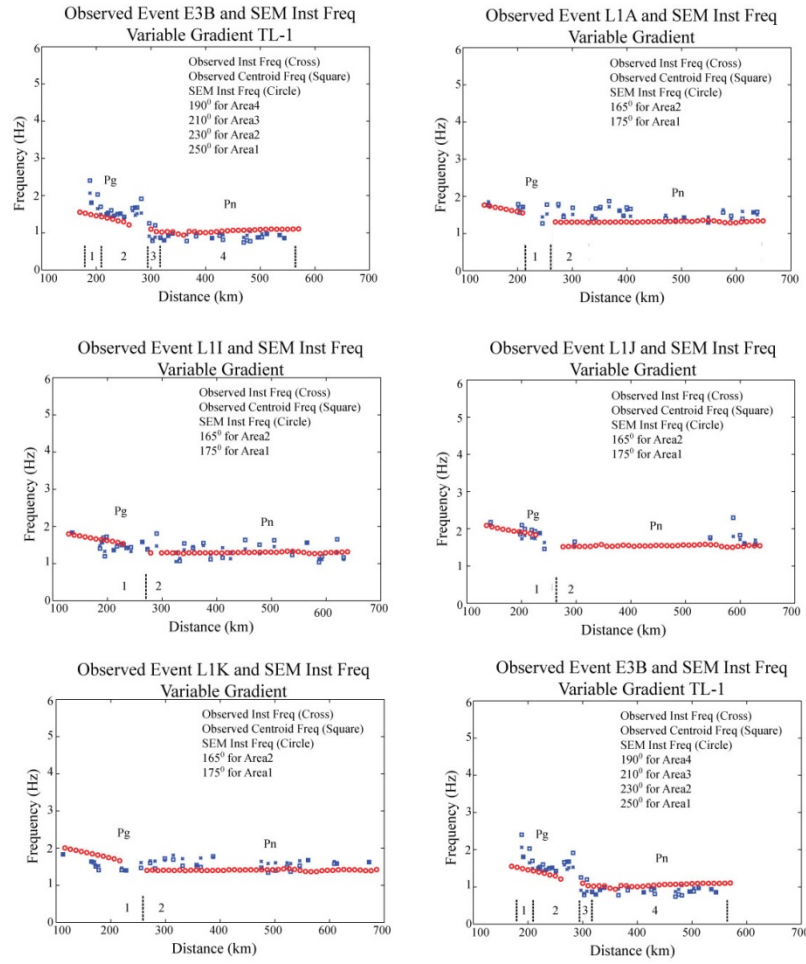


Figure 28. These plots show the instantaneous pulse frequencies of the selected events with a constant attenuation and a variable upper mantle velocity gradient for the SEM models compared with the observed instantaneous and centroid frequencies. The circles are the SEM calculations and the crosses and squares are observed instantaneous and centroid frequencies.

8. SEISMIC PROFILING WITH TELESEISMIC WAVES

In an effort to better constrain the structural model for the region, we have also completed several studies of large-scale, north-south variations in crustal thickness across the Tibetan plateau using teleseismic waves. Tseng et al. (2009) devised a new approach using the *SsPmp* phase for constructing deep-penetrating seismic profiles from teleseismic data which reveal significant, regional variations in crustal thickness under near-constant elevation of Tibet.

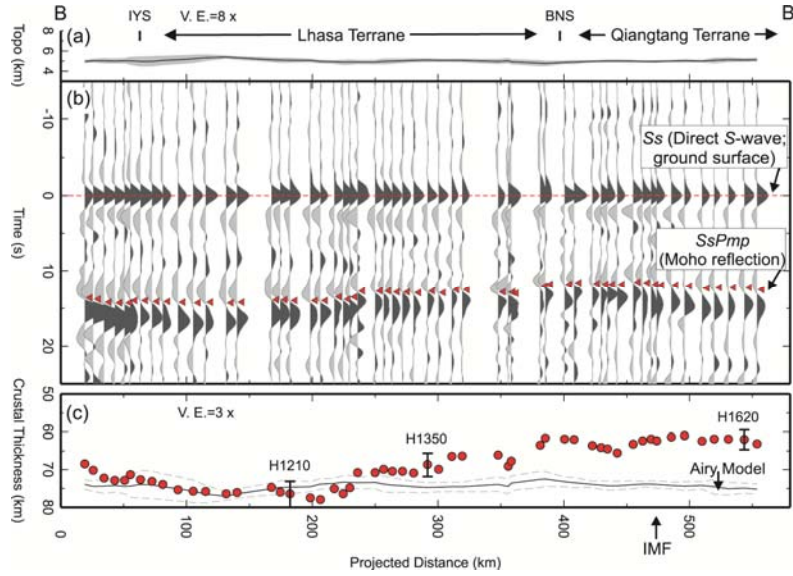


Figure 29. North-south trending profile across southern and central Tibet, showing topography on top, a P-wave reflection profile constructed using the phase *SsPmp*, and the estimated crustal thickness (Panels a, b, c, respectively).

The *SsPmp* phase originates as the direct *S*-wave (*Ss* phase) reflects under the free surface and partially converts to *P*-wave, which in turn reflects off the top of the Moho before finally arriving at a seismic station. The key concept is that the *P*- to *S*- conversion point below the free surface is a virtual source for the subsequent, reflected *P*-wave. In this view, the *SsPmp* phase is equivalent to the prominent “*PmP*” phase in a conventional seismic profile. Considering all known sources of error in this approach, the overall final uncertainty of crustal thickness is no more than about ± 3 km (over a total thickness of about 70 km, or $\pm 4\%$).

The very thick crust under Tibet is by no means uniform, instead there is an overall trend of northward thinning. The Moho reaches its deepest depth, up to 73–77 km, beneath the southern Lhasa terrane but shoals to around 60–64 km beneath the Qiangtang terrane. This regional variation in crustal thickness has a profound effect on the propagation of the *Pn* phase, and has been incorporated into the three-dimensional model of the lithosphere for detailed modeling of the frequency-dependent propagation of the *Pn* phase. Figure 29 shows a north-south trending profile across southern and central Tibet, showing topography on top, a pseudo *P*- wave reflection profile constructed using the *SsPmp* phase, and the estimated crustal thickness (Panels a, b, c, respectively).

We also conducted Gaussian beam migration of teleseismic receiver functions (Nowack et al., 2010). This approach allows for better resolution than traditional piercing point imaging using receiver functions. Figure 30 shows a comparison between crustal thickness estimated from wide-angle *P*-wave reflections from modeling the *SsPmp* phases (dots) and an image of the Tibetan lithosphere obtained from Gaussian beam migration of direct *P*- to *S*-wave conversions (from Tseng et al., 2009; and the Gaussian beam migration from Nowack et al., 2010).

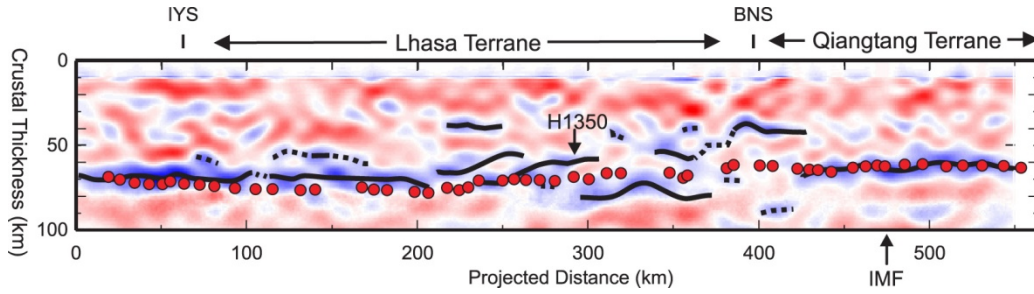


Figure 30. A comparison between crustal thickness estimated from wide-angle P-wave reflections (dots) from the teleseismic *SsPmp* phase and an image of the Tibetan lithosphere obtained from Gaussian beam migration of direct P- to S-wave conversions (from Tseng et al., 2009; and the Gaussian beam migration from Nowack et al., 2010).

Thinner crust under northern Tibet has been taken as evidence for full isostasy being achieved below the lithosphere, deep in the upper mantle where temperature is anomalously high. Supporting evidence for such a mechanism includes less efficient propagation of *Sn* waves just below the Moho, and large birefringence of S-waves (up to 2 s or more between fast- and slow-directions of polarization) that has been inferred as a result of east-west flow in the upper mantle. While our findings are generally consistent with this interpretation in a broad sense, there are preliminary indications that variations in properties of the uppermost mantle are too abrupt to be accounted for by thermal effects alone.

Finally, Hung et al. (2010) and Hung et al. (2011) have developed in detail, both the theory and the practice of an innovation that combines finite-frequency (“banana-doughnut”), travel-time tomography and a data-adaptive, multi-scale approach. When applied to the teleseismic *P*- and *S*-wave data, collected under Project Hi-CLIMB, this new method yields high-resolution results in the uppermost mantle where both lateral and radial variations in *P*- and *S*-wave speeds are resolved over an area of approximately 700 by 400 km in central and southern Tibet. This result provides an independent comparison of the velocity structure beneath the Hi-CLIMB array.

9. CONCLUSIONS

We have investigated frequency-dependent characteristics of *Pn* propagation over a large region in western China based on numerous events recorded by the Hi-CLIMB array from this region. Attributes of seismic wave-trains, including arrival times, Hilbert envelope amplitudes, and instantaneous and spectral frequencies, have been modeled to investigate how structures in the crust and the upper mantle affect the propagation of the *Pn* phase in Tibet. For the modeling, we applied 3D ray methods, as well as the spectral element method which provides complete numerical solutions in laterally varying media. The objective was to obtain self-consistent models of *Pn* propagation in western China which are free from assumptions, such as frequency-independent geometric spreading. To this end, our results should advance efforts in isolating effects of frequency-dependent

propagation from those of pure-inelastic attenuation (Q), leading to improved methodologies for discrimination and yield estimates at regional distances.

We first modeled P -wave arrival-times to constrain the velocity structure in the crust and the upper mantle in central and western Tibet. Travel-times from four events along the Hi-CLIMB array provided details on crustal velocities, and six events at regional distances to the array provide further constraints on Moho structure and upper mantle lid velocities. We used 3D ray tracing to model the travel-times, and the results indicated that both Moho structure and mantle-lid velocities in the region are three-dimensional in nature but approximately follow the trend of the Bangong-Nujiang Suture (BNS). Although only a limited number of events were used for the travel-time modeling, the results are consistent with earlier results from teleseismic imaging using the Hi-CLIMB array.

We then modeled P_n wave attributes, including envelope amplitudes and pulse frequencies, recorded by the Hi-Climb array in Tibet. Three 2D P -wave velocity slices for the events were used in the SEM calculations. All the slices were then earth-flattened for use in the 2D SEM calculations. The SEM modeling of the pulse amplitudes and frequencies suggested a variable upper mantle structure in which the Qiangtang terrane has higher attenuation than the Lhasa terrane in the upper mantle. However, the modeling with a constant upper mantle attenuation structure also shows that this can provide a good fit to the observed amplitudes and frequencies, but only if a variable velocity gradient structure exists with a lower velocity gradient beneath the Qiangtang terrane compared to the Lhasa terrane.

Thus, two alternative models for the region are found, one with a constant upper mantle velocity gradient similar to those of Griffin et al. (2011) and Phillips et al. (2007) with a variable attenuation model and one with a constant attenuation model and a variable upper mantle velocity gradient similar to that of Myers et al. (2010). In either case, the upper mantle of the Qiangtang terrane can be distinguished from the Lhasa terrane. The lower P_n velocities and lower P_n amplitudes suggest hotter temperatures in the upper mantle beneath the Qiangtang terrane compared to the Lhasa terrane. Either lower Q_p values or a lower upper mantle velocity gradient in the Qiangtang terrane compared to the Lhasa terrane can be used to match the seismic attribute data presented here.

10. RECOMMENDATIONS

Since structural velocity models can have substantial effects on the frequency dependent propagation of P_n waves, it is recommended that these effects be further studied using adequately sampled seismic array data from regional events. This then can be used to establish baselines for specific locations for discrimination and yield estimates at regional distances. However, more work is needed to investigate trade-offs between spatially varying attenuation models and complex velocity models. Along with more complicated structural models, frequency variable Q models from small-scale scattering also need to be incorporated into the modeling of P_n waves.

REFERENCES

- Aki, K. and P. G. Richards (2002). Quantitative seismology, Volume I, W. H. Freeman, San Francisco.
- Bakir, A. C. (2011). Modeling of seismic Pn attributes using the spectral element method for velocity and attenuation structure of the Tibetan lithosphere, M.S. thesis, Purdue University, West Lafayette, IN, 179 pp.
- Baur, J. R. (2007). Seismotectonics of the Himalayas and the Tibetan Plateau: Moment tensor analysis of regional seismograms, M.S. thesis, Oregon State Univ., 275 pp.
- Birch, F. 1964, Density and composition of the mantle and core, *J. Geophys. Res.* 69: 4377-4387.
- Bracewell, R. N. (2000). The Fourier transform and its applications, McGraw-Hill Boston, pp. 359-360.
- Braile, L. W. and R. B. Smith (1975). Guide to the interpretation of crustal refraction profiles, *Geophys. J. R. Astr. Soc.* 40: 145–176.
- Cerveny, V., L. Klimes, and I. Psencik (1988). Complete seismic-ray tracing in three-dimensional structures, in *Seismological Algorithms*. London: Academic Press.
- Cerveny, V. and R. Ravindra (1971). *Theory of Seismic Head Waves*. University of Toronto Press.
- Chen, M., J. Tromp, D. Helmberger and H. Kanamori (2007), Waveform modeling of the slab beneath Japan, *J. Geophys. Res.*, **112**, B02305.
- Chen, W.-P., and P. Molnar (1983). Focal depths of intracontinental and intraplate earthquakes and their implications for the thermal and mechanical properties of the lithosphere, *J. Geophys. Res.* 88: 4183–4214.
- Chen, W. P. M. Martin, T. L. Tseng, R. L. Nowack, S. Hung, and B. Huang (2010). Shear-wave birefringence and current configuration of converging lithosphere under Tibet, *Earth Planet. Sci. Lett.* 295: 297-304.
- Chew, W. C. (1990). Waves and fields in inhomogeneous media, Nostrand Reinhold Book Co., pp. 57-66.
- Dahlen, F. A. and J. Tromp (1998). Theoretical global seismology, Princeton University Press, pp. 327-350.
- Dziewonski, A. M., T.-A. Chou and J. H. Woodhouse (1981). Determination of earthquake source parameters from waveform data for studies of global and regional seismicity, *J. Geophys. Res.* 86: 2825–2852.
- Engdahl, E. R., R. D. van der Hilst, and R.P. Buland (1998). Global teleseismic earthquake relocation with improved travel times and procedures for depth determination, *Bull. Seism. Soc. Am.* 88: 722–743.

- Griffin, J. D., R. L. Nowack, W. P. Chen and T.L. Tseng (2011). Velocity structure of the Tibetan Lithosphere: Constraints from *P*-wave travel times of regional earthquakes, *Bull. Seism. Soc. Am.*, in press.
- Helmberger, D. and J. E. Vidale (1988), Modeling strong motions produced by earthquakes with two-dimensional numerical codes, *Bull. Seism. Soc. Am.* 78: 109-121.
- Hill, D. (1971). Velocity gradients and anelasticity from crustal body-wave amplitudes, *J. Geophys. Res.* 76: 3309–3325.
- Hill, D. (1973). Critically refracted waves in a spherically symmetric radially heterogeneous Earth model, *Geophys. J. R. Astr. Soc.* 34: 149–177.
- Hung, S. H., W. P. Chen, L. Y. Chiao, and T. L. Tseng (2010). First multi-scale, finite frequency tomography illuminates 3-D anatomy of the Tibetan Plateau, *Geophys. Res. Lett.* 37: doi:10.1029/2009GL041875.
- Hung, S.-H., W.-P. Chen, and L.-Y. Chiao (2011). A data-adaptive, multi-scale approach of finite-frequency, travel-time tomography with special reference to *P*- and *S*-Wave data from central Tibet, *J. Geophys. Res.*, submitted.
- Klein, F. (2002). HYPOINVERSE-2000 (4/2002 vers.). [Computer Software]. Menlo Park, CA: U.S. Geological Survey.
- Komatitsch, D. and J. P. Vilotte (1998). The spectral element method: An efficient tool to simulate the seismic response of 2D and 3D geological structures, *Bull. Seismol. Soc. Am.* 88: 368–392.
- Komatitsch, D., S. Tsuboi, and J. Tromp (2005). The spectral-element method in seismology, in *Seismic Earth: Array Analysis of Broadband Seismograms*, Geophysical Monograph Series, Vol. 157, A. Levander and G. Nolet, Eds. Washington, DC: American Geophysical Union.
- Langin, W. R., L. D. Brown, and E. A. Sandvol (2003). Seismicity of central Tibet from Project INDEPTH III seismic recordings, *Bull. Seism. Soc. Am.* 93: 2146–2159.
- Matheney, M. and R. L. Nowack (1995). Seismic attenuation values obtained from instantaneous frequency matching and spectral ratios, *Geophys. J. Int.* 123: 1-15.
- Menke, W. H. and P. G. Richards (1980). Crust-mantle whispering gallery phases—A deterministic model of teleseismic Pn wave-propagation, *J. Geophys. Res.* 85: 5416–5422.
- Miksat, J., T. M. Muller and F. Wenzel (2008), Simulating three-dimensional seismograms in 2.5-dimensional structures by combining two-dimensional finite difference modeling and ray tracing, *Geophys. J. Int.* 174: 309-315.
- Molnar, P. and W.-P. Chen (1983). Depths and fault plane solutions of earthquakes under the Tibetan plateau, *J. Geophys. Res.* 88: 1180–1196.
- Myers, S. M. L. Begnaud, S. Ballard, M. E. Pasyanos, W. S. Phillips, A. L. Ramirez, M. S. Antolik, K. D. Hutchenson, J. J. Dwyer, C. A. Rowe, and G. S. Wagner (2010).

- A crust and upper-mantle model of Eurasia and North Africa for P_n travel-time calculation, *Bull. Seism. Soc. Am.* 100: 640–656.
- Nabelek, J., W. P. Chen, M. R. Pandey, J. Mei, J. Chen, B. S. Huang, and the Project Hi-CLIMB Team (2005). Hi-CLIMB: A high-resolution seismic profile across the Himalayas and Southern Tibet, IRIS Annual Report, Washington DC.
- Nowack, R. L. and S. M. Stacy (2002), Synthetic seismograms and wide-angle seismic attributes from the Gaussian beam and reflectivity methods for models with interfaces and velocity gradients, *Pure Applied Geophys.* 159: 1447-1464.
- Nowack, R. L., W. P. Chen, and T. L. Tseng (2010). Application of Gaussian beam migration to multi-scale imaging of the lithosphere beneath the Hi-CLIMB array in Tibet, *Bull. Seism. Soc. Am.* 100: 1743-1754.
- Phillips, W. S., M. L. Begnaud, C. A. Rowe, L. K. Steck, S. C. Myers, M. E. Pasyanos, and S. Ballard (2007). Accounting for lateral variations of the upper mantle gradient in P_n tomography studies, *Geophys. Res. Lett.* 34: doi:10.1029/2007GL029338.
- Sereno, T. J. and J. W. Given (1990). P_n attenuation for a spherically symmetric Earth model, *Geophys. Res. Lett.* 17: 1141–1144.
- Tseng, T. L., W. P. Chen, and R. L. Nowack (2009). Northward thinning of the Tibetan crust revealed by virtual seismic profiles, *Geophys. Res. Lett.* 36: L244304, doi:10.1029/2009GL040457.
- Vidale, J., D. V. Helmberger and R. W. Clayton (1985). Finite-difference seismograms for SH waves, *Bull. Seism. Soc. Am.* 75: 1765-1782.
- Yang, X., T. Lay, X. B. Xie, and M. S. Thorne (2007). Geometric spreading of P_n and S_n in a spherical earth model, *Bull. Seism. Soc. Am.* 97: 2053–2065.

APPENDIX A. CALCULATION OF SEISMIC ATTRIBUTES

Let $s(t)$ be a seismic wavelet, then the analytical signal $a(t)$ can be written as

$$a(t) = s(t) + i \tilde{s}(t) \quad (\text{A.1})$$

where

$$\tilde{s}(t) = \frac{1}{\pi} \int_{-\infty}^{\infty} \frac{s(\tau) d\tau}{\tau - t} \quad (\text{A.2})$$

is the Hilbert transform (Bracewell, 2000). The analytical signal in the time domain can also be written as

$$a(t) = e^{i\phi(t)} \quad (\text{A.3})$$

where the instantaneous amplitude (trace envelope) is given by

$$e(t) = (s^2(t) + \tilde{s}^2(t))^{1/2}, \quad (\text{A.4})$$

and the instantaneous phase is

$$\phi(t) = \tan^{-1} \left(\frac{\tilde{s}(t)}{s(t)} \right). \quad (\text{A.5})$$

The instantaneous frequency is then given by

$$f(t) = \frac{1}{2\pi} \frac{d}{dt} (\phi(t)). \quad (\text{A.6})$$

This can also be calculated as

$$f(t) = \frac{1}{2\pi} \frac{s(t) \frac{d\tilde{s}(t)}{dt} - \tilde{s}(t) \frac{ds(t)}{dt}}{e^2(t) + \varepsilon^2} \quad (\text{A.7})$$

where damping, ε^2 , is used to stable the instantaneous frequency when the envelope amplitude is small. This is less important here since the instantaneous frequencies are evaluated at the peak of the envelope amplitude of the extracted Pg and Pn pulses. In addition, as the windowed average of the instantaneous frequency weighted by the squared envelope becomes larger, the estimate approaches the centroid of the power spectrum, where the frequency integral is over the positive frequencies (Nowack and Stacy, 2002; Matheney and Nowack, 1995).

An example of a data trace from the Hi-Climb array and a windowed trace and envelope are shown in figure A.1. For the pulse, the amplitude is taken at the peak of the

Hilbert envelope. The instantaneous frequency is also taken at the time where the peak of Hilbert envelope occurs. The centroid frequency is taken from the Fourier transform of the windowed seismic pulse. If the envelope doesn't sufficiently drop after the first arriving pulse, the trace is not included for further amplitude and frequency analysis (Matheney and Nowack, 1995). Also, if the estimated instantaneous frequency is not consistent with the adjacent traces in distance, then the trace is not included under the assumption that the pulse has been contaminated with later arrivals. Both the observed and the calculated data are analyzed using the same processing steps.

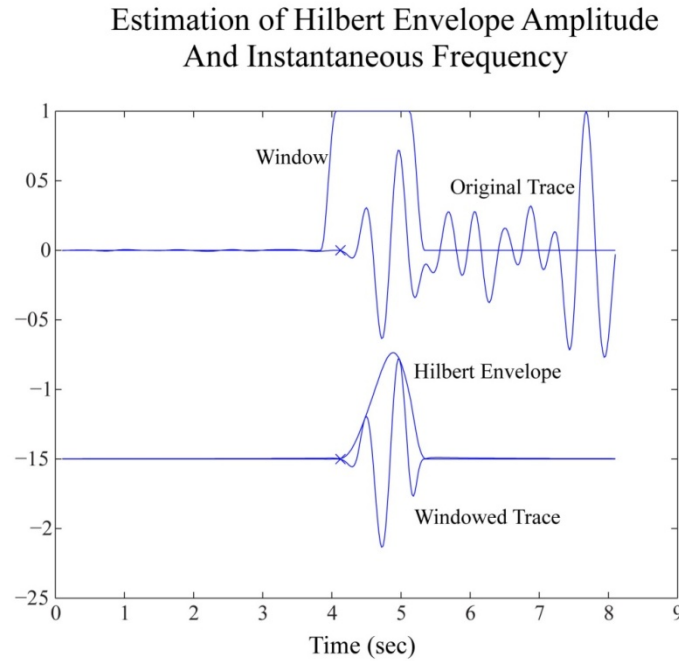


Figure A1. This shows an example of a data trace from the Hi-CLIMB array with a window function at the top and a windowed trace and envelope at the bottom.

APPENDIX B. VALIDATION OF THE SPECTRAL ELEMENT METHOD FOR PN WAVES

In order to test the spectral-element method (SEM), comparisons are made between wide-angle seismic results obtained using SEM and the reflectivity results of Braile and Smith (1975), as well as, between the SEM and the asymptotic results of Cervený and Ravindra (1971). For these comparisons, in addition to the synthetic seismograms, various seismic attributes of the Pn are derived, including pulse amplitudes and pulse frequencies. The SEM calculations are implemented using the parallel code SPECFEM2D (Komatitsch and Vilotte, 1998; Komatitsch et al., 2005).

We first compare the SEM with reflectivity calculations. For various wide-angle applications, the reflectivity method has been used extensively to compute synthetic seismograms in vertically varying media. For example, Braile and Smith (1975) computed synthetic seismograms using the reflectivity method, and then examined the effects of various velocity-depth models on the calculated seismic waves. One of the results of the reflectivity calculations was the determination of wide-angle reflection arrivals from the Moho, PmP , and head-wave arrivals, Pn .

The velocity gradient below the Moho is an important parameter for the characterization of the Earth's upper mantle since it greatly affects Pn amplitudes. In addition, the flattening of a spherical Earth for calculation purposes will result in an effective positive velocity gradient below the Moho. As a result, an effective positive velocity gradient is prevalent. A positive velocity gradient results in diving waves and interference head-waves, while a negative velocity gradient strongly decays the amplitudes of head-waves (Hill, 1971).

To make a correct comparison between the SEM and the reflectivity results, the pulse shapes of the initial sources for each method must be the same. In the reflectivity calculations of Braile and Smith (1975), the source time function is given by

$$s(t) = \begin{cases} \sin(\delta t) - \frac{1}{m}\sin(m\delta t) & \text{where } 0 \leq t \leq \tau \\ 0 & \text{where } t < 0 \text{ and } t > \tau, \end{cases} \quad (\text{B.1})$$

with

$$\delta = \frac{N\pi}{\tau}, \quad m = \frac{N+2}{N}, \quad (\text{B.2})$$

where N is an integer also used to define the number of extrema of the pulses, where Braile and Smith (1975) used $N = 2$. τ is the duration in seconds of the source wavelet, and t is the sampled time (Fig. B.1), where Braile and Smith (1975) used $\tau = 0.2$ sec. In the SEM modeling, the first derivative of a Gaussian distribution is chosen to provide a

similar source pulse shape (Fig. B.1). The initial source time function in the SEM calculations is given by

$$s(t) = -2A(\pi^2 a_0^2) e^{-\pi^2 a_0^2 (t-t_0)^2} \quad (\text{B.3})$$

where A is a multiplication factor, a_0 is related to the width of the source time function, and t_0 is the time delay (Fig. B.1). In order to make these pulses similar, $a_0 = 7.4$ is found to be appropriate for the SEM source time function.

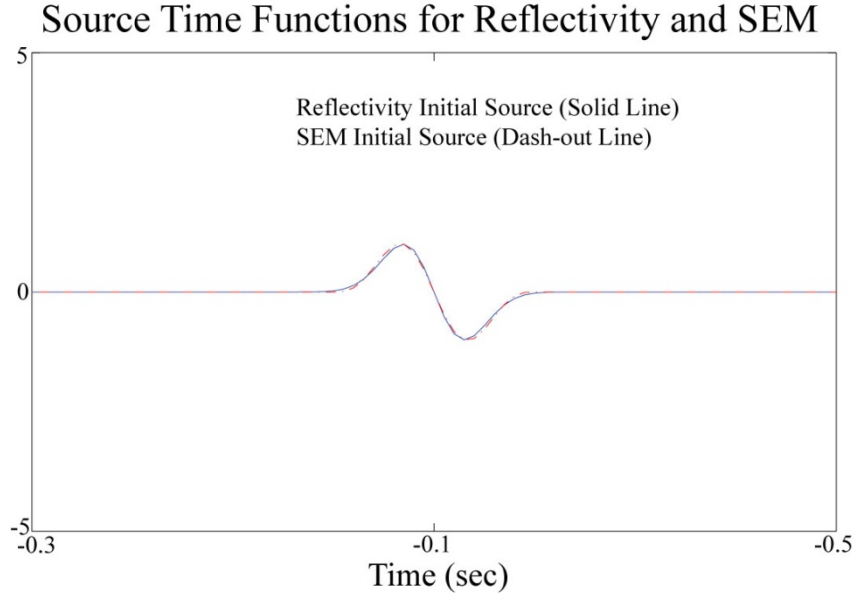


Figure B.1. Source time functions for the reflectivity calculation (solid line) with $\tau = 0.2$ sec and the SEM calculation with $a_0 = 7.4$ (dashed line).

Amplitudes of the seismograms vary in a different manner for 2D and 3D seismic wave propagation problems (Chew, 1990). Reflectivity method amplitudes from Braile and Smith (1975) are calculated for 3D, while SEM amplitudes are calculated for 2D wave solutions, and the amplitude variations with distance are different. In the 2D SEM, the source can be considered as a line source. Since the problem has cylindrical symmetry, this can be written in cylindrical coordinates as $U(x, y) = U(R)$ and $\delta(x)\delta(y) = \delta(R)$ (Chew, 1990), where R is the distance from the source. Assuming that $U(R)$ has a time dependence $e^{-i\omega t}$, amplitudes far from the source can be written as

$$U(R) \sim C \sqrt{\frac{2}{i\pi k R}} e^{ikR} \quad (\text{B.4})$$

where $C = i/4$, $k = \omega/\alpha_1$, and α_1 is the wave speed. Therefore 2D amplitudes can be written as

$$U(R) \sim \frac{i}{4} \sqrt{\frac{2}{i \pi k R}} e^{i k R} \quad (\text{B.5})$$

By substituting i with $e^{i\pi/2}$ and $\sqrt{1/i}$ with $e^{-i\pi/4}$ in Eqn (B.5), we can obtain the following equation for 2D amplitude variations in the frequency domain in the far field as

$$U(R) \sim \frac{1}{4} \sqrt{\frac{2\alpha_1}{\pi \omega R}} e^{i\pi/4} e^{i\omega R/\alpha_1} \quad (\text{B.6})$$

An important point here is that the exponential term $e^{i\omega R/\alpha_1}$ in the equations above results in a delay of the pulse in time. Because Matlab routines are used to make all corrections and Matlab uses a different sign convention in the frequency domain than Chew (1990), in terms of a time delay for a pulse, these exponential terms must have negative sign in Matlab implementation.

In the 3D reflectivity method, the source can be considered as a point source. Chew (1990) defines a point source in the frequency domain as

$$U(R) = \frac{1}{4\pi R} e^{i k R} = \frac{1}{4\pi R} e^{i\omega R/\alpha_1} \quad (\text{B.7})$$

In order to correct the 2D SEM amplitudes for 3D reflectivity, one needs to multiply the 2D SEM amplitudes by

$$\frac{1}{\pi} \sqrt{\frac{\pi \omega}{2\alpha_1 R}} (e^{-i\pi/4}). \quad (\text{B.8})$$

In a Matlab implementation, this correction has to be done with a reverse sign on the exponential.

$$\frac{1}{\pi} \sqrt{\frac{\pi \omega}{2\alpha_1 R}} (e^{i\pi/4}) \quad (\text{Matlab}). \quad (\text{B.9})$$

In Matlab, multiplying the 2D SEM amplitudes by the term in Eqn. (B.9), we obtain the corrected amplitudes of 2D SEM for comparison with the 3D reflectivity. After this correction is done, amplitudes of both methods are multiplied by distance for plotting purposes. Although, this is correct for homogeneous media, it will still correct the 2D calculations for approximate out of plane spreading for a medium only varying in a 2D plane. Higher order asymptotic corrections from 2D to effective 3D are given by Miksat et al. (2008) as well as other work by Vidale et. al (1985), Helmberger and Vidale (1988) and Chen et. al (2007).

Synthetic Seismograms for Model Moho-1 (Vertical Components) Original SEM Amplitudes with no Corrections (top) and with Pulse Shape and Corrections (bottom)

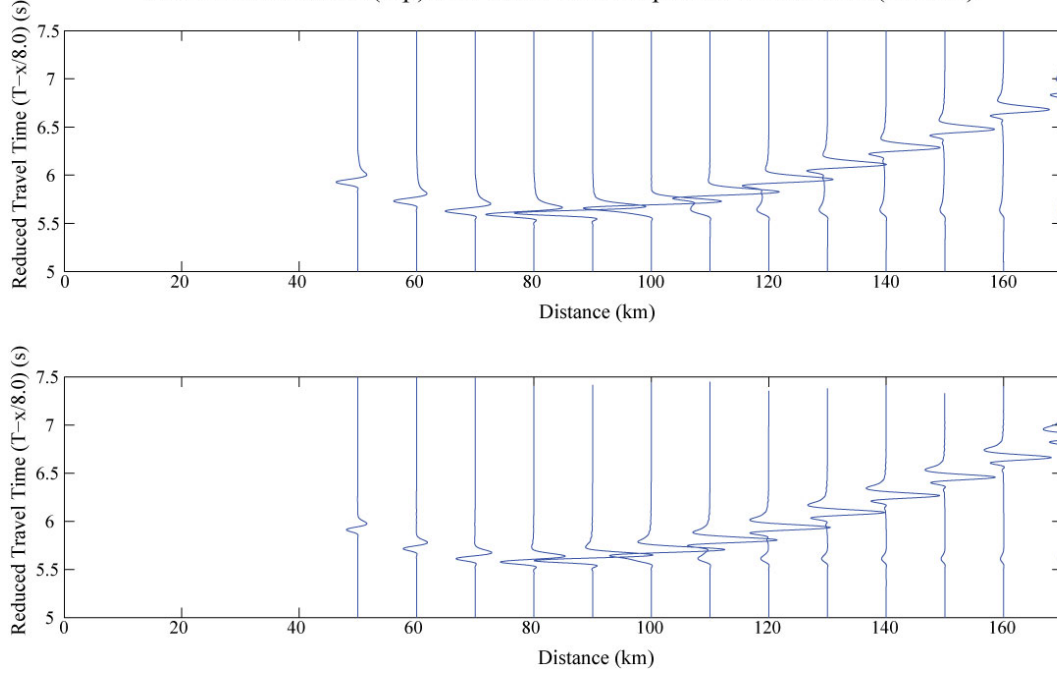


Figure B.2. SEM synthetics of model Moho-1 with no 3D correction (top) and SEM synthetics of model Moho-1 with 3D distance and pulse shape corrections (bottom). Top and bottom amplitudes are scaled by the maximum amplitude of all traces.

The first comparison is for a constant velocity 30 km crust over a constant velocity mantle, and is called Moho-1 by Braile and Smith (1975). The P-wave velocity in the crust α_1 is 6.4 km/sec and the P-wave velocity in the mantle α_2 is 8.0 km/sec. The S-wave velocities β_i of the layers are computed assuming a Poisson ratio = 0.25. The densities are computed from $\rho_i = 0.252 + 0.3788\alpha_i$ (Birch, 1964 and Braile and Smith, 1975). In figure B.2, the SEM calculations for Moho-1 are shown. In the top plot, the SEM synthetics are scaled by the maximum amplitude of all traces. The bottom plot shows the SEM synthetics multiplied by the Eqn (B.9) in the frequency domain for a 3D amplitude correction, then scaled by the maximum amplitude of all traces. These two plots show how the pulse shapes vary between 2D and 3D calculations. In figure B.3, a plot of the results of Braile and Smith (1975) for Moho-1 (solid line) and those from the corrected results of SEM (dashed line) are shown. Both results are multiplied by distance for plotting purposes. As can be seen from the comparison, the results are in good agreement.

Synthetic Seismograms for Model Moho-1 (Vertical Component)

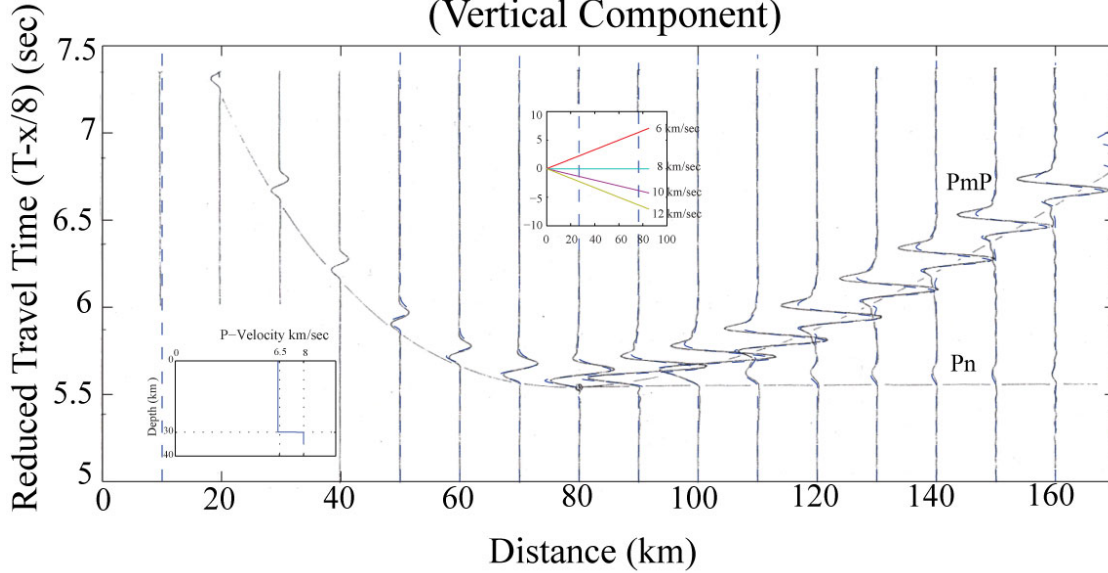


Figure B.3. A comparison between the SEM calculations (dashed) and the reflectivity results (solid) of Braile and Smith (1975) for a constant velocity 30 km crust over a constant velocity mantle. The amplitudes of the reflectivity results and the 3D corrected SEM results are both multiplied by distance in the plot.

The second comparison model is a constant velocity 30 km crust over a positive velocity gradient in the top 5 km of the mantle, and is named Moho-5 by Braile and Smith (1975). The P-wave velocity of the crust α_1 is 6.4 km/sec which is the same as Moho-1. However, the velocity gradient in the upper mantle for 5 km below the Moho is calculated by $\alpha_2(z) = \alpha_2^{top} + bz$ where α_2^{top} is the top velocity of the mantle (8 km/sec), b is the velocity gradient (0.08sec^{-1}), and z is the depth. At the depth of 35 km, the velocity of the mantle is 8.4 km/sec and this velocity is constant down to the bottom of the model (60 km). The computation of the S-wave velocities and densities are done in the same manner as the Moho-1 model shown above. Similar to the Moho-1 model, the comparisons between the reflectivity results of Braile and Smith (1975) and those from the corrected SEM results are in good agreement (figure B.4).

For the Moho-1 model, figure B.3 shows that sub-critical reflections (less than 80 km in distance) reproduce the initial source time function. For the region around the critical distance, because the reflected waves and head-waves begin interfering, larger amplitude arrivals start appearing. There is a zone around the critical distance that larger amplitudes can be observed. The size of this zone depends on the frequency content of the source and lower frequencies will cause a larger sized zone (Braile and Smith, 1975). In figure B.3 and B.4, wide-angle reflections can easily be observed since they have the largest amplitudes compared to the other arrivals. Recalling that the travel times are reduced 8 km/sec and by looking at the given velocity slope chart in the figures, it can be seen that wide-angle reflections have an apparent velocity of 6.4 km/sec which is the upper homogeneous layer's velocity. In figures B.3 and B.4, the P_n amplitudes for the Moho-5 model are much larger than the head-wave amplitudes for the Moho-1 model.

Synthetic Seismograms for Model Moho-5 (Vertical Component)

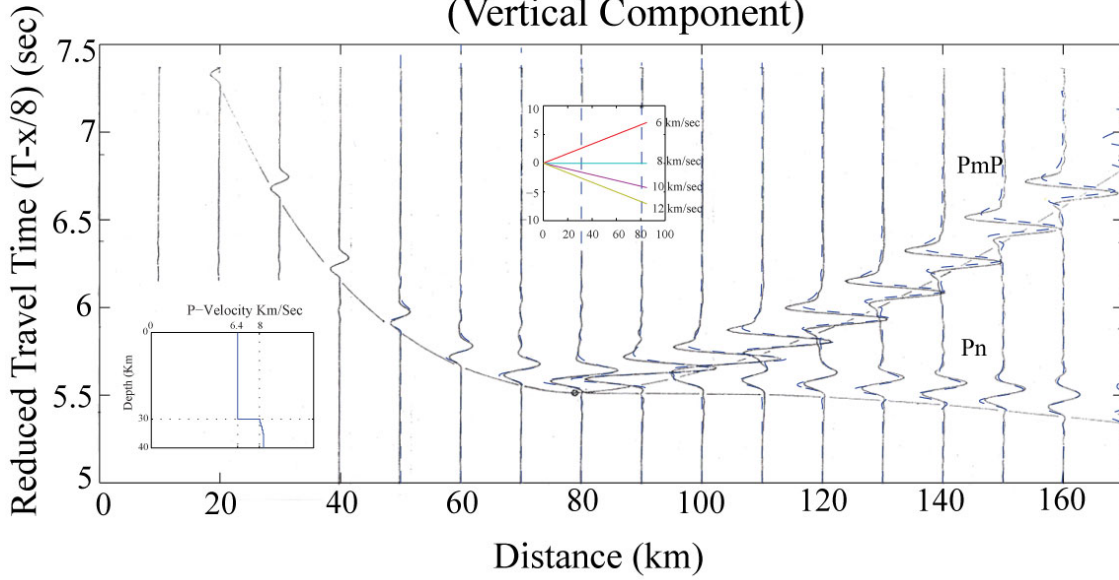


Figure B.4. A comparison between the results from the SEM calculations (dashed) and the reflectivity results (solid) of Braile and Smith (1975) for a constant velocity 30 km crust over a mantle with a velocity gradient in the top 5 km. Amplitudes of the reflectivity results and the corrected SEM results are both multiplied by distance in the plot.

This effect is due to the presence of a positive velocity gradient below the interface (Hill, 1971). In figure B.4, interference head-waves start appearing at distances where the pure head-waves are observed. In general, interference head-waves have very similar travel-time characteristics to the pure head-waves, but curve for greater distances. However, the amplitude characteristics of interference head-waves are quite different from the pure head-wave amplitudes (Braile and Smith, 1975).

SEM is next compared with the asymptotic results of Cerveny and Ravindra (1971). Only one interface is considered, and source and the receivers are located in the first medium. The pure head wave case of Cerveny and Ravindra is equivalent to the Moho-1 model given above of Braile and Smith (1975). The pure head wave case has a constant velocity 30 km crust over a constant velocity mantle model. Also, P-wave velocity in the crust is 6.4 km/sec and in the mantle is 8 km/sec which are identical to the Moho-1 model of Braile and Smith (1975). Cerveny and Ravindra (1971) chose the densities of different layers to be the same $\rho_1 / \rho_2 = 1$. The interference head wave case of Cerveny and Ravindra (1971) is a constant velocity 30 km crust over a positive velocity gradient mantle. The velocity in the lower medium is given by $\alpha_2(z) = \alpha_2^{top} + bz$ to calculate the velocity gradient where α_2^{top} is the top velocity of the mantle (8 km/sec) b is the velocity gradient ($0.002264 \text{ sec}^{-1}$), and z is the depth.

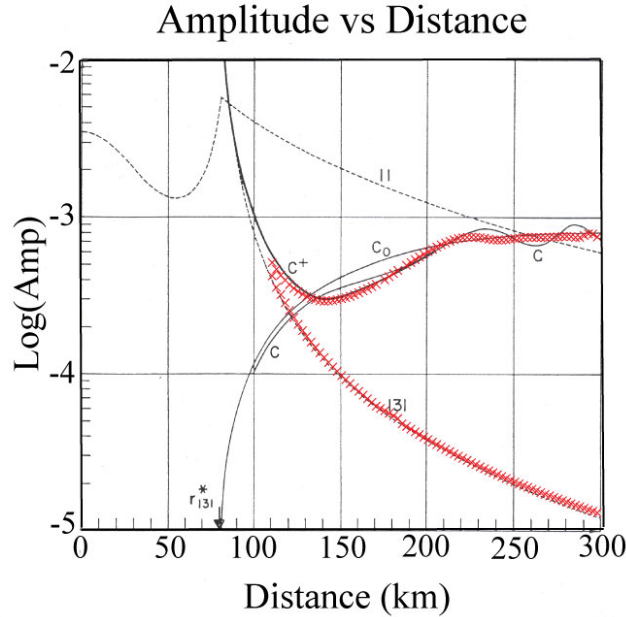


Figure B.5. This shows a comparison between the SEM calculations (crosses) and the asymptotic calculations (background plot) of Cerveny and Ravindra (1971) for the pure and interference head waves. C^+ wave is the interference head wave, C_0 is the diving wave, and the 131 wave is the pure head wave case (Modified background plot from Cerveny and Ravindra, 1971).

There is good agreement between asymptotic calculations of Cerveny and Ravindra (1971) and the SEM results for pure and interference head-wave cases. A positive velocity gradient below the interface drastically increases the head-wave amplitudes (Cerveny and Ravindra, 1971). Figure B.5 shows the comparison of the amplitudes of pure and interference head waves for the asymptotic calculations of Cerveny and Ravindra (1971) (background plot) and the SEM results (crosses). The pure head-wave case of Cerveny and Ravindra (1971) is referred to by 131 in figure B.5. Also the interference head-wave case of Cerveny and Ravindra (1971) is referred to by C^+ in figure B.5. Because the amplitude variations with distance are different for the 3D asymptotic method and 2D SEM (Chew, 1990) as mentioned above, the same amplitude correction in frequency domain has been made here for the 2D SEM results to compare with the 3D asymptotic results of Cerveny and Ravindra (1971).

The amplitude spectrum as a function of distance is given in figure B.6. The initial pulse has a dominant frequency of 6.4 Hz. The initial lowering of the centroid frequency of the spectra is at 140 km. Then the centroid frequency starts increasing. It then gets higher than the incident wave centroid frequency at 180 km. For greater distances, the diving waves begin to dominate. The emergence of the diving waves causes a lowering of the centroid frequency making it similar to the incident wave centroid frequency again. This is consistent with the asymptotic Gaussian beam calculations of Nowack and Stacy (2002). However, there is a tuning effect between different interference wave types, and this can result in an overshoot to higher frequencies for the centroid frequency.

Interference Head Wave Model

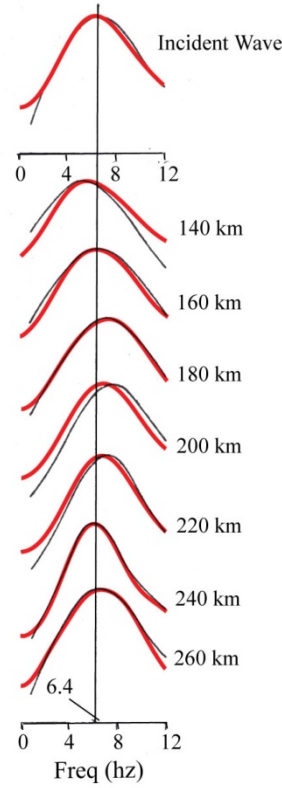


Figure B.6. This shows amplitude spectra as a function of distance for the interference head wave case. The thin black curves are from Cerveny and Ravindra (1971) and the thicker curves are from SEM calculations for the same model (Background plot from Cerveny and Ravindra, 1971).

The SEM is finally compared with an analytical solution for an attenuating medium. Amplitudes and pulse shapes in an attenuating medium are different from the amplitudes in an elastic medium, since amplitudes decay exponentially due to the attenuation. Aki and Richards (2002) give the amplitude decay in frequency for an attenuating medium with a constant Q as;

$$U(x, \omega) = U_0(\omega) e^{-\frac{\omega R}{2\alpha Q}} \quad (\text{B.10})$$

where $\omega = 2\pi f$, R is the distance, α is the velocity of the medium, Q is the quality factor of the medium, and $U(x, \omega)$ is the attenuated amplitude. Note that this attenuation filter will give an acausal operator and an added phase term is needed for a causal filter (Aki and Richards, 2002). However this is suitable for testing amplitudes and amplitude spectral shapes. To test the attenuation of the SEM, a homogeneous viscoelastic model with a Q_p of 112.5, a P-wave velocity of 5 km/sec, and a dominant frequency of 2 Hz is calculated for various source receiver distances. The synthetic traces of the SEM are compared with the analytical calculations for the same Q value applied in the Eqn (B.10).

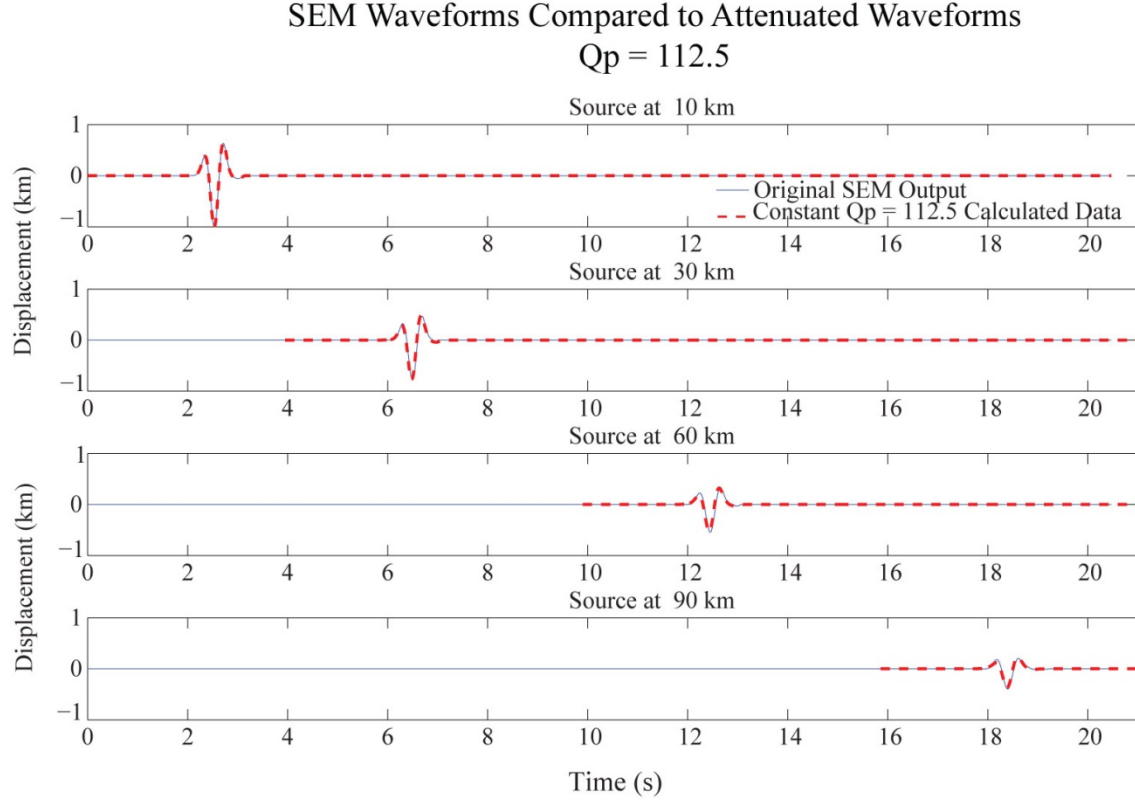


Figure B.7. This shows the comparison of the SEM traces with the analytical calculations for a homogeneous viscoelastic model with a Q_p of 112.5.

For this test, a receiver is put at the surface and four shots at different depths vertically below the receiver are used to calculate the SEM synthetics. Then, the SEM synthetics are compared with a constant Q (acausal) filter applied to the near distance SEM trace at 10 km depth. For this test, the bulk attenuation is neglected by using a large Q_κ value ($Q_\kappa = 1000$) and the Poisson's ratio is assumed to be 0.25 ($\alpha^2 / \beta^2 = 3$) in Eqn (B.11) (from Dahlen and Tromp, 1998).

$$\frac{1}{Q_p} = \left(1 - \frac{4\beta^2}{3\alpha^2}\right) \frac{1}{Q_\kappa} + \frac{4}{3} \left(\frac{\beta^2}{\alpha^2}\right) \frac{1}{Q_\mu} \quad (\text{B.11})$$

where α and β are the P and S wave velocities of the media. Then Q_μ , equal to Q_s , is chosen to be 50 resulting in a Q_p of 112.5 from the ratio of $Q_p = 9Q_s / 4$ between Q_p and Q_s for a large Q_κ . In order to retain this ratio, all SEM calculations in the following chapters are made based on assuming attenuation loss in shear. Figure B.7 shows the original SEM traces compared with the analytically calculated traces. Because an acausal Q model was used, the analytic traces were aligned with the SEM traces to highlight the effects of pulse broadening and amplitude decay. Figure B.8 shows the envelope amplitudes of the original SEM outputs compared with the envelope amplitudes of the

analytically calculated traces. Figure B.9 shows the frequency spectrum comparisons of the original SEM traces with the analytically calculated traces.

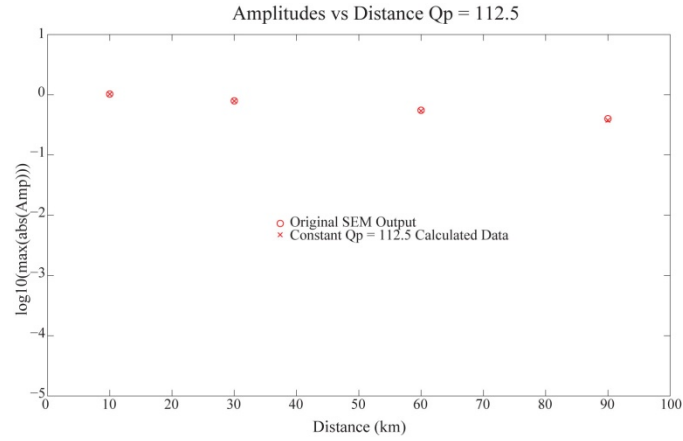


Figure B.8. This shows the envelope amplitude of the SEM traces with the envelope amplitude of the analytically calculated traces given in figure B.7.

Frequency Spectra for $Q_p = 112.5$

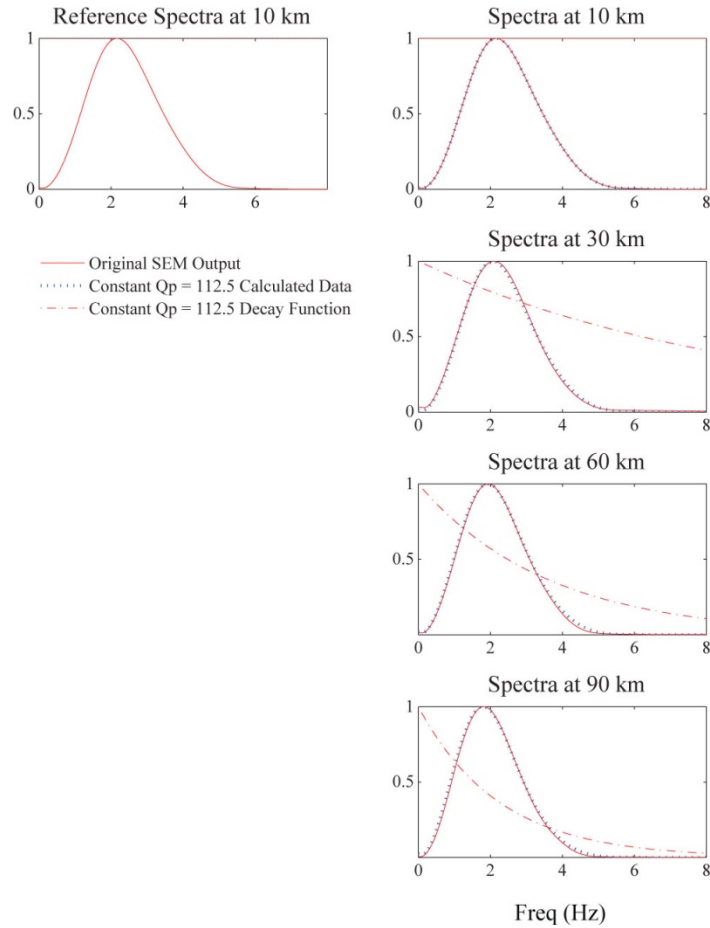


Figure B.9. This shows a comparison of the frequency spectra of the SEM traces with analytical calculations for the traces given in figure B.7.

In this appendix, synthetic seismograms using the SEM approach are compared with the reflectivity results from Braile and Smith (1975) and the asymptotic calculations of Cervený and Ravindra (1971). These comparisons show that the SEM approach can handle homogeneous, inhomogeneous and viscoelastic models, where very similar results are obtained from the SEM compared to the other approaches. However a correction for out-of-plane spreading is needed to compare 2D and 3D results in the case of only 2D variations in the medium as used here. For a positive velocity gradient below the Moho, an interference head-wave will result, and the amplitude and frequency characteristics can be quite different than the pure head-wave case.

**Velocity Structure of the Tibetan Lithosphere: Constraints
from *P*-Wave Travel Times of Regional Earthquakes**

By

Jessica D. Griffin, Robert L. Nowack*, Wang-Ping Chen and Tai-Lin Tseng

*Corresponding Author
Robert L. Nowack
Dept. of Earth and Atmos. Sciences
Purdue University
West Lafayette IN 47907 USA
Email : nowack@purdue.edu
Phone : 765-494-5978

Accepted to Bull. Seism. Soc. Am.

January 22, 2011

Abstract

Using data from regional earthquakes recorded by the Hi-CLIMB array in Tibet, we model *P*-wave arrival-times to constrain the velocity structure in the crust and the upper mantle in central and western Tibet. Of more than 30 high-quality, regional seismic profiles that have been assembled, we have selected 10 which show excellent crustal and *P_n* arrivals for further analysis. Travel times from four events along the Hi-CLIMB array provide details on crustal velocities, and six events at regional distances to the array provide further constraints on Moho structure and upper mantle lid velocities. We use 3-D ray tracing to model the travel times, and the results indicate that the Moho beneath the Lhasa terrane of southern Tibet is over 73 km deep with a *P_n* speed of about 8.2 km/s. The Qiangtang terrane north of the Bangong-Nujiang suture (BNS) shows a thinner crust, by up to 10 km, and a lower *P_n* speed of 7.8-7.9 km/s. Travel times from events to the west and east of the array indicate that both Moho structure and mantle-lid velocities in the region are three-dimensional in nature but approximately follow the trend of the BNS. Although only a limited number of events were used for the travel time modeling, the results are consistent with earlier results from teleseismic imaging using the Hi-CLIMB array.

Introduction

The Himalayan-Tibetan orogeny is the largest active continent-continent collision zone in the world (Yin and Harrison, 2000), and the continuing convergence has resulted in large scale deformation in central Eurasia (Molnar and Tapponnier, 1975; Tapponnier et al., 2001). The Hi-CLIMB (Himalayan-Tibetan Continental Lithosphere During Mountain Building) experiment was conducted along a north-south corridor between 84°E and 86°E extending from the Ganga foreland basin, over the Lesser and Higher Himalayas, crossing the Indus-Yarlung suture and the Bangong-Nujiang suture, then reaching into the Qiangtang terrane in central Tibet (Figure 1). Between 2002 to 2005, the Hi-CLIMB array was deployed in 3 phases with a total of over 210 broadband sites (Nabelek et al., 2005). A unique feature of the Hi-CLIMB experiment is that it crosses the highest portions of the Himalayas from the Indian shield to the interior of Tibet. It also has a unique combination of a dense station spacing of 3 to 8 km for the main linear array and a broad regional coverage. In this study we investigate data from the linear array component of Hi-CLIMB in Tibet to analyze first arrival travel times from regional earthquakes.

Because of the importance of the region for understanding active continental collision, Tibet has been the site of several large scale field experiments in recent years (e.g. Hirn et al., 1984; Zhao et al., 1993; McNamara et al., 1994; Kind et al., 2002; Tilmann et al., 2003; Wittlinger et al., 2004, 2009). Studies of *P_n* in Tibet have found thicknesses of roughly double the continental average (Chen and Molnar, 1981; Hearn et al., 2004; and Liang et al., 2004, 2006; Sun and Toksoz, 2006).

Using teleseismic data from the Hi-CLIMB experiment, the crust was found to be between 70 and 80 km thick beneath the Lhasa terrane, but on the order of 10 km thinner

beneath the Qiangtang terrane to the north (Nabelek et al., 2009; Tseng et al., 2009; Nowack et al., 2010). From the analysis of wide-angle and teleseismic data from the INDEPTH III experiment located about 5 degrees to the east of Hi-CLIMB but crossing similar terranes, a somewhat smaller change in crustal thickness was found from south to north (Zhao et al., 2001; Kind et al., 2002; Shi et al., 2004; Tian, et al., 2005). While the Moho conversion is distinct and coherent beneath a majority of both the Lhasa and Qiangtang terranes from receiver function images of Hi-CLIMB data images, the conversion strength was observed to vary with the direction of illumination (Nabelek et al., 2009; Nowack et al., 2010). Also from Hi-CLIMB data, a zone of crustal and Moho disruption marks the Bangong-Nujiang suture (BNS) zone between the more stable Lhasa and Qiangtang blocks (Nowack et al., 2010).

From travel time studies, the average P_g velocities in the Tibetan crust was found to be lower than the continental average, in the range of 6.2 to 6.3 km/s (Zhao et al., 2001; Monsalve et al., 2008; Steck et al., 2009). Studies from the Hi-CLIMB and INDEPTH experiments, which have more dense station spacings, found similar average crustal velocities. Also, lower crustal velocities were found in the areas of the Indus-Yarlung suture (IYS) and the Bangong-Nujiang suture (BNS) for Hi-CLIMB (Hung et al., 2010) and in the area of the BNS for INDEPTH III (Haines et al., 2003; Meissner et al., 2004).

Upper mantle P -wave velocities beneath Qiangtang terrane north of the BNS were found from regional travel time studies to be as low as 7.9 km/s (Liang et al., 2004; Hearn et al., 2004; Pei et al., 2007). These low velocities, as well as the inefficient S_n propagation observed in this area (Barazangi and Ni, 1982; Ni and Barazangi, 1983; Brandon and Romanowicz, 1986; McNamara and Owen, 1995; McNamara et al., 1997; Xie et al., 2004; Barron and Priestley, 2009), imply that the thinner crust of the Qiangtang terrane is at least in part isostatically supported by a mantle beneath that is hotter and more buoyant (Zhao et al., 2001; Jimenez-Munt et al., 2008). The P -wave velocities inferred beneath the southern Tibetan Plateau, south of the Bangong-Nujiang suture, are as high as 8.3 km/s and similar to the upper mantle velocities observed beneath stable cratonic regions, such as the Indian shield or the Tarim and Sichuan basins (McNamara et al., 1997; Liang and Song, 2006; Pei et al., 2007).

The differences between results from Hi-CLIMB and INDEPTH III highlight the fact that, while the Tibetan Plateau is composed of a succession of terranes from north to south (Dewey et al., 1988), there exists significant lateral variation from west to east, and the structure of the plateau must be taken into account in all three dimensions. In this study, forward modeling of P -wave travel times from regional earthquakes recorded by the linear array component of Hi-CLIMB in Tibet is used to determine the three-dimensional P -wave velocity structure for the region of the central and western Tibetan Plateau beneath the Hi-CLIMB array.

Data Analysis

We used broadband seismic data from regional earthquakes in Tibet recorded by the densely spaced, linear component of the Hi-CLIMB array in Tibet (Figure 1) to investigate crustal and upper mantle structure. Based on locations of epicenters reported in the EHB catalog (Engdahl et al., 1998, see Data and Resources) or the NEIC PDE catalog (USGS, See Data and Resources; for events not included in the EHB), we selected events for which both P_g and P_n arrivals were recorded by the Hi-CLIMB array in Tibet (Figure 1; a list of events is available as an electronic supplement to this paper).

To construct a velocity model along the trend of the Hi-CLIMB array in Tibet, we relied on data from four events located along and nearby the array (L2a, L2d, L3a, and L3b; Figure 1) for crustal structure. In addition, we used six events whose epicenters are about 200 to 300 km away from the nearest station to constrain seismic velocity structures in the crust and the upper mantle on a regional scale. Four of the events to the south of the array have similar epicenters. This provides some verification on the variation in the P -wave travel times due to small-scale heterogeneity as well as picking errors. The entire group of events was selected to be largely in-line with the trend of the array, but also to provide a range of azimuthal coverage. We visually picked the timing of the first P -arrivals on the vertical component of the broadband seismograms after applying a six-pole, Butterworth band-pass filter between 0.5 and 5.0 Hz. The average pick error is estimated to be ± 0.3 s. Figure 2 shows examples of seismic record-sections from two events with the traces plotted with respect to surface distance of the event to each station, and all travel times are reduced by 8.0 km/s.

We carried out forward modeling of the travel times using a 3D ray tracing code by Cerveny et al. (1988; the CRT algorithm). In doing so, the elevation of the free surface in the model is at 5 km above sea-level, the average elevation of the Hi-CLIMB stations. The model consists of a grid system, with a spacing of 1° in longitude, 0.5° in latitude, and 10 km in depth, over the region between 27 to 36°N in latitude and 80 to 90°E in longitude and extending down to a depth of 200 km. The Moho is an explicit surface separating grid-points in the crust from those in the upper mantle. A scheme of cubic splines interpolate among the nodes of the grid system to specify values of seismic wave speeds and positions of the Moho and to calculate ray paths in the three-dimensional model. An example of the 3D ray tracing for event L1e is shown in Figure 3.

Earthquake Events along the Hi-CLIMB Array

The epicenters for earthquakes L2a, L2d, L3a, and L3b are located along the length of the Hi-CLIMB array in Tibet (Figure 1), and the P_g travel times recorded from these nearby sources are used to constrain the crustal velocity structure beneath the array. The four events were first relocated using the location code HYPOINVERSE 2000 (Klein, 2002), and the relocated epicenters range from 4 to 15 km distant from the reported epicenters (see the electronic supplement for a table of the relocated hypocenters for the nearby events). Also, while the reported depths of these sources are between 15

and 19 km below the surface, their depths changed to 6–15 km below the surface after relocation, which are more consistent with the shallow crustal seismogenic zone in Tibet (Chen and Molnar, 1983; De la Torre et al., 2007).

For the sources along the array, it can be observed in Figure 4 that the slopes of the *Pg* branches for all four events are generally linear both to the north and to the south of each source. The apparent velocities implied by the slopes of the *Pg* branches are between 5.9 and 6.1 km/s. Modeling of the *Pg* travel times for these events was first done using an initial 1D crustal model (Figure 4A, solid line) derived from an average crustal model of Meissner et al. (2004) for the INDEPTH III experiment, but with somewhat slower velocities in the mid to lower crust as inferred by the linear slopes of the observed *Pg* arrivals for Hi-CLIMB. Fig 4B shows the observed *P*-wave travel times for the relocated events L2a, L2d, L3a, and L3b compared with the travel times calculated using the initial 1D crustal velocity model. All travel times are reduced by 8.0 km/s and plotted with respect to the minimum recorded travel time rather than an absolute origin time whose precise value is unknown. In Figs. 4B and 4C, the origin position of each event on the x-axis is determined by its projected position along the linear trend of the Hi-CLIMB array. But, as with the record sections, the *P*-wave travel times are plotted in either direction away from the source position as a function of epicentral distance from the source to each receiver.

Although the initial 1D crustal velocity model does a reasonable job of fitting the travel times, there are still some mismatches between the observed and calculated travel times. The misfit between the observed and calculated travel times can be seen in Figure 4B for event L2a at distances less than -400 km and greater than -100 km on the x-axis, for L2d at distances less than -300 km and greater than +50 km on the x-axis, and for L3b at distances less than -50 km on the x-axis. This indicates that there is some additional lateral variability in the crustal velocities along the profile of the array. Therefore, starting from the initial 1D velocity profile, a refined crustal velocity model was obtained that includes a reduction of up to 0.15 km/s or by around 3 percent from the initial 1D crustal model in the top 30 km of the crust to the north of latitude 33.5°N and to the south of latitude 31°N.

Figure 4C compares the observed and calculated travel times for the refined crustal velocity model and shows that the reduced velocities beneath the southern and northern portions of the array provide a better fit to the observed travel times at far offsets. The observed *Pg* travel times for event L3a are well fit by the calculated travel times using the refined crustal velocity model, and the value of RMS misfit for the *Pg* travel times is only 0.25 s, smaller than average picking error. The refined crustal velocity model also produces a good fit between the observed and calculated *Pg* travel times for event L3b, and the average misfit of *Pg* arrivals is 0.29 s. For event L2a, the observed *Pg* travel times at far offsets are well fit by those calculated for the refined crustal velocity model and results in an RMS misfit of 0.24 s for crustal arrivals. The observed travel times to the north of event L2d are generally well matched by the calculated travel times for the refined crustal velocity model, but the observed *Pg* travel times for stations to the south are still somewhat later than those calculated. Also, the

observed travel times of L2d are earlier than those calculated for this model between offsets of 75 to 200 km to the north which could possibly be due to the presence of a localized zone of high velocity. However this is not observed in the travel times for other sources recorded at the same stations, so while the average value of RMS misfit of 0.43 s is slightly larger than the average picking error, a crustal model which provides a better fit for travel times at these offsets for event L2d would not be consistent with the data observed from the other events. Nonetheless, the refined crustal velocity model provides the best average fit to the *Pg* travel times for all the events along the array.

While the *Pn* branches recorded for the nearby events shown in Figure 4 are typically short and have a lower signal-to-noise ratio, the *Pg* to *Pn* crossover distances can offer some initial constraints on the depth of the Moho along the Hi-CLIMB array. The *Pg* to *Pn* crossover distances for the events L2a, L3a, and L3b are observed at epicenter distances in the range of 250 to 300 km and are consistent with crustal thicknesses of up to 73 km in the south beneath event L3a but with a thinner crust to the north beneath event L3b. The Moho depths of the refined crustal velocity model can be constrained by the observed *Pg* to *Pn* crossover distances of these two events, as well as the observed *Pn* branches of the more regional events located farther from the array. While not all the observed *Pn* travel times for event L2a are well fit, there is some uncertainty in the *Pn* picks for this event and there is a possibility that these arrivals were picked late or on a different phase. However, this could also result from additional three-dimensional complications in the derived Moho model.

Earthquakes at Far Regional Distances from the Hi-CLIMB Array

Six far regional earthquakes recorded by the Hi-CLIMB array in Tibet were selected to study *Pn* velocities and Moho depths to determine the velocity structure of the crust and upper mantle in the region. The events shown on Figure 1 were selected which have prominent *Pn* arrivals, as well as some *Pg* arrivals so that the crossover distance is included. While these events are located too far from the Hi-CLIMB array to be effectively relocated, the depths were estimated to be consistent with the observed *Pg* to *Pn* cross-over distances for each event, and the Moho depths inferred from the nearby events and other far regional events. (available as an electronic supplement to this paper; see also, Griffin, 2010).

The observed *P*-wave travel times for the regional earthquakes are shown in Figure 5. In Figure 5A the observed travel times for event L1e show that the *Pg* travel times are consistent with the average velocities of around 6.0 km/s inferred from the four events nearby the Hi-CLIMB array. It can be seen that the *Pn* travel times for stations at distances between 250 and 450 km are delayed in comparison with those at distances greater than 500 km to the north of the event. Travel time modeling indicates that the Moho is deeper in the southern portion of the model at a depth of around 73 km and shallower to the north at a depth of around 64 km. The slope of the *Pn* branch to the south can be modeled by upper mantle velocities and velocity gradients of around 8.3 km/s and 0.004 s^{-1} , respectively. The slope of the *Pn* branch to the north can be modeled by upper mantle velocities and velocity gradients of 7.8 km/s and 0.003 s^{-1} , respectively.

The P_n travel time curve for event L1e shows a transition between 400 and 550 km from the source and indicates that the transition between the deeper Moho in the south and the shallower Moho to the north occurs over a horizontal distance of roughly 150 km between the latitudes of 31° and 32.5°N . The value of the RMS misfit between the observed and calculated travel times for this event using the inferred 3D regional velocity model (Figures 6 and 7) is 0.27 s. Some of the misfit might suggest further complications on the P_n speeds away from the Hi-CLIMB array. However, here a self-consistent velocity model among all the seismic gathers is developed.

Figure 5B shows the observed travel times for event L1a located to the south of the Hi-CLIMB array. As with event L1e, the observed P_g travel times are consistent with the crustal velocities observed using the four nearby events to the Hi-CLIMB array. The observed P_g to P_n crossover distance and P_n travel times indicate Moho depths, upper mantle velocities, and velocity gradients with values in the south and the north similar to those found for event L1e. The P_n travel times are consistent with the a northward shallowing of the Moho occurring over a distance of roughly 150 km between the latitudes 31° and 32.5°N , similar to L1e.

These results also agree with the data from events L1i, L1j, and L1k with epicenters located near event L1a and are shown in Figures 5(c), (d) and (e). Since these events have similar epicentral locations, they provide a good assessment of the overall data quality. The value of RMS misfit between the observed travel times and the calculated travel times for event L1a using the 3D regional velocity model (Figures 6 and 7) is 0.16 s and similar values were found for events L1i, L1j, and L1k.

Event E3b is located to the northeast of the Hi-CLIMB array and Figure 5(f) shows the observed travel times for this event. The calculated P_g travel times agree with the observed travel times using the refined crustal velocity model determined from the four events located nearby the array. The observed P_n travel times indicate Moho depths, upper mantle velocities, and velocity gradients with values in the south and north parts of the model similar to those found for the other far regional events. However, the transition between P_n travel times in the north and in the south, shown by the bar in Figure 5(f), indicates that the Moho shallows northward over a slightly longer distance of around 200 km and slightly farther to the south between the latitudes of 30° and 32°N . The regional velocity model determined in this study (Figures 6 and 7) results in an RMS misfit between the calculated and observed travel times for this event of 0.26 s. Some of the misfit could result from additional variations in the P_n speeds away from the Hi-CLIMB array, and also in the vicinity of the transition in Moho depth near the BNS.

Results and Discussion

Using 3D ray tracing (Cerveny et al., 1988; the CRT algorithm) to forward model the P_g and P_n travel times, we have determined a 3D P -wave velocity model for the crust and upper mantle in the central and western Tibetan Plateau. Figure 6(a) illustrates the crustal velocities found beneath the Hi-CLIMB array which varies laterally from north to south with slightly lower velocities in the crust observed in the areas of the IYS and north

of the BNS. Figure 7 highlights the velocity structure of the upper mantle and shows that upper mantle velocities of around 8.3 km/s and crustal thicknesses of close to 73 km are found beneath the southern portion of the Tibetan Plateau. To the north of the BNS in the Qiangtang terrane, upper mantle velocities are found to be lower at around 7.8 km/s, and the crust in this area is about 10 km thinner than that observed to the south.

The separation between the Lhasa terrane to the south and the Qiangtang terrane to the north can also be observed in receiver function images from Hi-CLIMB (Nabelek et al., 2009; Nowack et al., 2010) as a disruption in the Moho conversion in the receiver function images to the south of the BNS. The location of this disruption coincides with the transition in the Moho depth and upper mantle velocities found in this study. Figure 6(b) shows a comparison of the Moho depth results in this study (gray line) from wide-angle travel time modeling using regional events with the teleseismic imaging results of Nowack et al. (2010), where the solid lines are the interpreted locations of the subsurface Moho and other structures. Tseng et al. (2009) also determined Moho depths from virtual wide-angle seismic profiles using teleseismic data and their wide-angle imaging results are consistent with the results of this study using regional wide-angle events. While the results from geologic mapping and balanced cross-sections given in Kapp et al. (2005) and Ding et al. (2007) suggest a northward dipping suture near the surface between the Lhasa and Qiangtang terranes, the results of this and other geophysical studies from Hi-CLIMB (Tseng et al., 2009; Nowack et al., 2010) find a zone of changing Moho depth which suggests a geophysical suture at depth mainly located to the south of the surface expression of the BNS which could imply a southward dipping suture between the Lhasa and the Qiangtang terranes.

Regional tomography studies have found lower than average P_g and S_g velocities in the Tibetan crust of around 6.1 and 3.4 km/s, respectively (Steck et al., 2009; Monsalve et al., 2008; Sun and Toksoz, 2006). Prior studies using both Hi-CLIMB and INDEPTH III data have also observed low velocity zones in the crust near the areas of the IYS and BNS (Hung et al., 2010; Meissner et al., 2004), which this is similar to the results found from this study for the crust. Also, the results for upper mantle P_n velocities found in this study are consistent with earlier studies of P_n in Tibet, including those of Hearn et al. (2004), Sun and Toksoz (2006), Liang and Song (2006), and Phillips et al. (2007).

The inferred upper mantle velocities and gradients from this study are consistent with those of Phillips et al. (2007) in Tibet with upper mantle velocity gradients in this region of Tibet between 0.003 s^{-1} to 0.004 s^{-1} . Myers et al. (2010) found similar upper mantle velocity gradients in southern Tibet, but lower gradients in the Qiangtang terrane in northern Tibet. However, their study was much larger in scale incorporating Eurasia and North Africa. For this study, the upper mantle velocities are well modeled by the regional travel time data, but the modeled upper mantle velocity gradients are less constrained (Griffin, 2010). For a better resolution of upper mantle velocity gradients, longer offsets than those used here would be needed, since the offsets in this study were restricted to include only events with well recorded cross-over distances between the P_g and P_n branches. Alternatively, other seismic attributes, such as P_n amplitudes, could be

used to provide better constraints on the upper mantle velocity gradients and is the subject of current research.

Although the event coverage in this study is limited, In addition to the north-south variation, the inferred velocity model also shows an east-west lateral variation. The location and width of the transition in Moho depth is largely constrained by the travel times for ray paths from the regional event L1e sampling mostly to the west of the Hi-CLIMB array and the travel times of the ray paths of event E3b sampling predominantly to the east of the array. To the west, the Moho is found to shallow to the north between the latitudes of 31° to 32.5°N , whereas to the east, the northward shallowing of the Moho is found to occur farther to the south between 30 to 32°N and generally follows the surface trend of the Bangong-Nujiang suture (BNS).

Conclusions

This study uses broadband seismic data recorded by the Hi-CLIMB array in central and western Tibet from earthquake sources located both along and at more regional distances from the Hi-CLIMB array. These events provide travel time data along the profile of the array but also afford some azimuthal coverage of the region. Observed *P*-wave travel times from selected regional earthquakes were modeled using 3D ray-tracing in order to determine the velocity structure of the crust and upper mantle structure in Tibet near the Hi-CLIMB array. Although only a limited number of events were used for the travel time modeling, the results are consistent with earlier results from teleseismic imaging beneath the Hi-CLIMB array.

A laterally varying refined crustal velocity model was found using *Pg* travel times from the events located along and nearby the Hi-CLIMB array, and the inferred velocities are similar to those given by Meissner et al. (2004) for INDEPTH III in the upper crust but with slower velocities in the mid to lower crust beneath the Hi-CLIMB array. Crustal velocities in the top 30 km of the crust were also found to be up to 0.15 km/s slower in the area of the Indus-Yarlung suture south of latitude 31°N and in the area of the Bangong-Nujiang suture north of latitude 33.5°N .

The *Pn* travel times observed for the more regional events to the Hi-CLIMB array were used to constrain the Moho structure and upper mantle velocities in the region. It was found that the crust is as thick as 73 km beneath the southern part of the plateau in the Lhasa terrane and about 10 km thinner beneath the northern area of the plateau in the Qiangtang terrane. This north-south variation is also present in the inferred variation in upper mantle velocities which were found to be about 8.3 km/s beneath the Lhasa terrane in the southern plateau, but as low as 7.8 km/s to the north of the BNS beneath the Qiangtang terrane. However the travel time data from events L1e to the west of the Hi-CLIMB array, and E3b to the east of the array, imply variations in the east-west direction as well, generally following the surface trend of the BNS. The transition from faster upper mantle velocities and a thicker crust in the south to slower upper mantle velocities and a thinner crust in the north occurs over a distance of 150 km between the latitudes of 31° and 32.5°N in the western portion of the velocity model and occurs over a distance

of around 200 km between the latitudes of 30° and 32°N in the eastern portion of the model.

Data and Resources

Seismic data used in this study were collected as part of the Hi-CLIMB Project using instruments from a number of different sources, including many from the Incorporated Research Institutions in Seismology-Program for the Array Seismic Studies of the Continental Lithosphere (IRIS-PASSCAL) Center. The project was organized and coordinated jointly by the University of Illinois (principal investigator, Wang-Ping Chen) and Oregon State University (principal investigator, John Nabelek). Seismic data can be obtained directly from the IRIS Data Management Center at www.iris.edu.

Ray tracing was performed using the 3D ray tracing code by Cerveny et al. (1988; the CRT algorithm), and event relocation was performed using the location code HYPOINVERSE-2000 (Klein, 2002).

The USGS/NEIC (PDE) earthquake locations are available at <http://earthquake.usgs.gov/earthquakes/eqarchives/epic/database.php> (last accessed, November 2010). The EHB catalog of earthquakes (Engdahl et al., 1998) is available at <http://www.isc.ac.uk/search/bulletin/ehb.html> (last accessed, October 2010).

Acknowledgements

This work was supported by the U.S. National Science Foundation grants EAR06-35419 (W. P.C., T.-L. T.), EAR06-35611 (R.L.N.), and the U.S. Air Force AFRL grant FA8718-08-C-002 (J.D.G, R.L.N., W.-P.C. and T.-L. T.).

References

- Barazangi, M. and J. Ni (1982) Velocities and propagation characteristics of *Pn* and *Sn* beneath the Himalayan arc and Tibetan plateau: evidence for underthrusting of Indian continental lithosphere beneath Tibet, *Geology* **10**, 179-185.
- Barron, J. and K. Priestley (2009). Observations of frequency-dependent *Sn* propagation in northern Tibet, *Geophys. J. Int.* **179**, 475-488.
- Brandon, C. and B. Romanowicz (1986). A no-lid zone in the central Chang-Thang platform of Tibet - Evidence from pure path phase-velocity measurements of long period Rayleigh waves, *J. Geophys. Res.* **91**, 6547-6564.
- Cerveny, V., L. Klimes, and I. Psencik (1988). Complete Seismic-Ray Tracing in Three-Dimensional Structures. In *Seismological Algorithms*, ed. D.J. Doornbos. Academic Press, London. 89-168.
- Chen, W.-P., and P. Molnar (1981). Constraints on the Seismic Wave Velocity Structure Beneath the Tibetan Plateau and Their Tectonic Implications, *J. Geophys. Res.* **86**, 5937-5962.
- Chen, W.-P., and P. Molnar (1983). Focal Depths of Intracontinental and Intraplate Earthquakes and Their Implications for the Thermal and Mechanical Properties of the Lithosphere, *J. Geophys. Res.* **88**, 4183-4214.
- De la Torre, T.L., G. Monsalve, A.F. Sheehan, S. Sapkota, and F. Wu (2007). Earthquake Processes of the Himalayan Collision Zone in Eastern Nepal and the Southern Tibetan Plateau, *Geophys. J. Int.* **171**, 718-738.
- Dewey, J.F., R.M. Shackleton, C. Chengfa, and S. Yiyin (1988). The Tectonic Evolution of the Tibetan Plateau. *Philosophical Transactions of the Royal Society of London. Series A, Mathematical and Physical Sciences* **327**, 379-413.
- Ding, L., P. Kapp, Y. Yue, and Q. Lai (2007). Postcollisional Calc-alkaline Lavas and Xenoliths from the Southern Qiangtang Terrane, Central Tibet, *Earth Planet. Sci. Lett.* **254**, 28-38.
- Engdahl, E.R., R. van der Hilst, and R. Buland (1998). Global Teleseismic Earthquake Relocation with Improved Travel Times and Procedures for Depth Determination, *Bull. Seism. Soc. Am.* **88**, 722-743.
- Griffin, J. D. (2010). Modeling of three-dimensional regional velocity structure using wide angle seismic data from the HI-CLIMB experiment in Tibet, M.S. Thesis, Purdue University, West Lafayette IN.
- Haines, S.S., S.L. Klemperer, L. Brown, G. Jingru, J. Mechie, R. Meissner, A. Ross, and Z. Wenjin (2003). INDEPTH III Seismic Data: From Surface Observations to Deep Crustal Processes in Tibet, *Tectonics* **22**, doi: 10.1029/2001TC001305.
- Hearn, T.M., S. Wang, J.F. Ni, Z. Xu, Y. Yu, and X. Zhang (2004). Uppermost Mantle Velocities Beneath China and Surrounding Regions, *J. Geophys. Res.* **109**, B11301.
- Hirn, A., A. Nercessian, M. Sapin, G. Jobert, Z.X. Xu, E.Y. Gao, D.Y. Lu, and J.W. Teng (1984). Lhasa Block and Bordering Sutures - A Continuation of a 500 km Moho Traverse Through Tibet, *Nature* **307**, 25-27.
- Hung, S.-H., Chen, W.-P., Chiao, L.-Y., Tseng, T.-L. (2010). First Multi-scale, Finite-frequency Tomography Illuminates 3-D Anatomy of the Tibetan Plateau, *Geophys. Res. Lett.* **37**, L06304.

- Jimenez-Munt, I., M. Fernandez, J. Verges, and J.P. Platt (2008). Lithosphere Structure Underneath the Tibetan Plateau Inferred from Elevation, Gravity and Geoid Anomalies, *Earth Planet. Sci. Lett.* **267**, 276-289.
- Kapp, P., P.G. DeCelles, A.L. Leier, J.M. Fabijanic, S. He, A. Pullen, and G.E. Gehrels (2007). The Gangdese Retroarc Thrust Belt Revealed, *GSA Today* **17**, 4-9.
- Kind, R., X. Yuan, J. Saul, D. Nelson, S.V. Sobolev, J. Mechie, W. Zhao, G. Kosarev, J. Ni, U. Achauer, and M. Jiang (2002). Seismic Images of Crust and Upper Mantle Beneath Tibet: Evidence for Eurasian Plate Subduction, *Science* **298**, 1219-1221.
- Klein, F. (2002). HYPOINVERSE-2000 (4/2002 vers.) [Computer Software]. Menlo Park, CA: U.S. Geological Survey.
- Liang, C., and X. Song (2006). A low Velocity Belt Beneath Northern and Eastern Tibetan Plateau from P_n Tomography, *Geophys. Res. Lett.* **33**, L22306.
- Liang, C., X. Song, and J.L. Huang (2004). Tomographic Inversion of P_n Travel Times in China, *J. Geophys. Res.* **109**, B11304.
- McNamara, D.E., T.J. Owens, P.G. Silver, and F.T. Wu (1994). Shear-Wave Anisotropy Beneath the Tibetan Plateau, *J. Geophys. Res.* **99**, 13655-13665.
- McNamara, D.E., T.J. Owens and W.R. Walter (1995) Observations of regional phase propagation across the Tibetan plateau, *Geophys. Res. Lett.* **100**, 22,215-22,219.
- McNamara, D.E., W.R. Walter, T.J. Owens, and C.J. Ammon (1997). Upper Mantle Velocity Structure Beneath the Tibetan Plateau from P_n Travel Time Tomography, *J. Geophys. Res.* **102**, 493-505.
- Meissner, R., F. Tilmann, and S. Haines (2004). About the Lithospheric Structure of Central Tibet, Based on Seismic Data From the INDEPTH III Profile, *Tectonophysics* **380**, 1-25.
- Molnar, P., and P. Tapponnier (1975). Cenozoic Tectonics of Asia - Effects of a Continental Collision, *Science* **189**, 419-426.
- Monsalve, G., A. Sheehan, C. Rowe, and S. Rajaure (2008). Seismic Structure of the Crust and the Upper Mantle Beneath the Himalayas: Evidence for Eclogitization of Lower Crustal Rocks in the Indian Plate, *J. Geophys. Res.* **113**, B08315.
- Myers, S.C., M.L. Begnaud, S. Ballard, M.E. Pasyanos, W.S. Phillips, A. L. Ramirez, M.S. Antolik, K.D. Hutchenson, J. J. Dwyer, C.A. Rowe, and G.S. Wagner (2010) A crust and upper-mantle model of Eurasia and North Africa for P_n travel time calculation, *Bull. Seism. Soc. Am.* **100**, 640-656.
- Nabelek, J., W.-P. Chen, M.R. Pandey, J. Mei, J. Chen, B.S. Huang, and the Project Hi-CLIMB Team (2005). Hi-CLIMB : A High-Resolution Seismic Profile Across the Himalayas and Southern Tibet. IRIS Annual Report., Washington D.C.
- Nabelek, J., G. Hetenyi, J. Vergne, S. Sapkota, B. Kafle, M. Jian, H. Su, J. Chen, and B.S. Huang (2009). Underplating in the Himalaya-Tibet Collision Zone Revealed by the Hi-CLIMB Experiment, *Science* **325**, 1371-1374.
- Ni, J. and M. Barazangi (1983). High-frequency seismic wave propagation beneath the Indian shield, Himalyan arc, Tibetan plateau and surrounding regions: high uppermost mantle velocities and efficient S_n propagation beneath Tibet, *Geophys. J. R. astr. Soc.* **72**, 665-689.
- Nowack, R.L., W.-P. Chen, and T.-L. Tseng (2010). Application of Gaussian Beam Migration to Multi-Scale Imaging of the Lithosphere Beneath the Hi-CLIMB Array in Tibet, *Bull. Seism. Soc. Am.* **100**, 1743-1754.

- Pei, S., J. Zhao, Y. Sun, X. Xu, S. Wang, H. Liu, C.A. Rowe, M.N. Toksoz, and X. Gao (2007). Upper Mantle Seismic Velocities and Anisotropy in China Determined Through P_n and S_n Tomography, *J. Geophys. Res.* **112**, B05312.
- Phillips, W.S., M.L. Begnaud, C.A. Rowe, L.K. Steck, S.C. Myers, M.E. Pasyanos, and S. Ballard (2007). Accounting for Lateral Variations of the Upper Mantle Gradient in P_n Tomography Studies, *Geophys. Res. Lett.* **34**, L14312.
- Shi, D., W. Zhao, L. Brown, D. Nelson, X. Zhao, J. Ni, J. Xiong, J. Mechie, J. Guo, S. Klemperer, and T. Hearn (2004). Detection of Southward Intracontinental Subduction of Tibetan Lithosphere Along the Bangong-Nujiang Suture by P-to-S Converted Waves, *Geology* **32**, 209-212.
- Steck, L.K., W.S. Phillips, K. Mackey, M.L. Begnaud, R.J. Stead, and C.A. Rowe (2009). Seismic Tomography of Crustal P and S Across Eurasia, *Geophys. J. Int.* **177**, 81-92.
- Sun, Y., and M.N. Toksoz (2006). Crustal Structure of China and Surrounding Regions from P Wave Traveltime Tomography, *J. Geophys. Res.* **111**, B03310.
- Tapponnier, P., Z.Q. Xu, F. Roger, B. Meyer, N. Arnaud, G. Wittlinger, and J.S. Yang (2001). Geology - Oblique Stepwise Rise and Growth of the Tibetan Plateau, *Science* **294**, 1671-1677.
- Tian, X., Q. Wu, Z. Zhang, J. Teng, and R. Zeng (2005). Joint Imaging by Teleseismic Converted and Multiple Waves and Its Application in the INDEPTH-III Passive Seismic Array, *Geophys. Res. Lett.* **32**, L21315.
- Tilmann, F., J. Ni, and the INDEPTH III Seismic Team (2003). Seismic Imaging of the Downwelling Indian Lithosphere Beneath Central Tibet, *Science* **300**, 1424-1427.
- Tseng, T.-L., W.-P. Chen, and R.L. Nowack (2009). Northward Thinning of Tibetan Crust Revealed by Virtual Seismic Profiles, *Geophys. Res. Lett.* **36**, L24304.
- Wittlinger, G., V. Farra, and J. Vergne (2004). Lithospheric and Upper Mantle Stratifications Beneath Tibet: New Insights from S_p Conversions, *Geophys. Res. Lett.* **31**, L19615.
- Wittlinger, G., V. Farra, G. Hetenyi, J. Vergne, and J. Nabelek (2009). Seismic Velocities in Southern Tibet Lower Crust: A Receiver Function Approach for Eclogite Detection, *Geophys. J. Int.* **177**, 1037-1049.
- Xie, J., R. Gok, J. Ni, and Y. Aoki (2004). Lateral Variations of Crustal Seismic Attenuation Along the INDEPTH III Profiles in Tibet from L_g Q Inversion, *J. Geophys. Res.* **109**, B10308.
- Yin, A., and T.M. Harrison (2000). Geologic Evolution of the Himalayan-Tibetan Orogen, *Annu. Rev. Earth Planet Sci.* **28**, 211-280.
- Zhao, W., J. Mechie, L.D. Brown, J. Guo, S. Haines, T. Hearn, S.L. Klemperer, Y.S. Ma, R. Meissner, K.D. Nelson, J.F. Ni, P. Pananont, R. Rapine, A. Ross, and J. Saul (2001). Crustal Structure of Central Tibet as Derived from Project INDEPTH III Wide-Angle Seismic Data, *Geophys. J. Int.* **145**, 486-498.
- Zhao, W.J., K.D. Nelson, and the INDEPTH Seismic team (1993). Deep Seismic-Reflection Evidence for Continental Underthrusting Beneath Southern Tibet, *Nature* **366**, 557-559.

Affiliations

Dept. of Earth and Atmos. Sciences
Purdue University
West Lafayette IN 47907 USA
(J.D.G & R.L.N.)

Dept. of Geology
University of Illinois-Urbana
Urbana IL 61801 USA
(W.-P. C. & T.-L. T.)

Now at Department of Geosciences
National Taiwan University
Taipei, Taiwan
(T.-L. T.)

Figure Captions

Figure 1. The topography of the Tibetan Plateau shown with the stations of the Hi-CLIMB array in Tibet (triangles) and the epicenters of the selected regional earthquake sources (circles). Black circles indicate the USGS/NEIC PDE and EHB reported hypocenters, and the white dots indicate the epicenters of the four events nearest to the array which have been relocated in this study. The locations of the Bangong-Nujiang suture (BNS) and the Indus-Yarlung suture (IYS) are shown by the dotted lines, and the solid line gives the reference line along the Hi-CLIMB array used for plotting the locations of the events L2a, L2d, L3a, and L3b as used in Figure 4.

Figure 2. Examples of vertical component record section recorded by the Hi-CLIMB array in central Tibet. (a) Shows the record section for earthquake L3a, and (b) shows the record section for earthquake L1e. On both record sections, the first arriving P_g or P_n waves are indicated. The waveforms were filtered with a six pole Butterworth bandpass filter between .5 and 5.0 Hz. The data are shown in reduced time by 8.0 km/s, and each trace is amplitude normalized. For each trace on the record sections, the first arrivals of P -waves are marked by black dots.

Figure 3. A rendering of the P -wave ray-paths calculated by the 3D ray-tracing code CRT (black lines) for the event L1e (white sphere) as viewed from the west. The gray surface indicates the structure of the Moho used within the input velocity model for the ray tracing.

Figure 4. (a) The initial 1D crustal velocity model (solid line) found for the region of Hi-CLIMB with upper crustal velocities similar to those found by Meissner et al. (2004) but with slower velocities in the mid to lower crust. (b) The observed travel times of the first arriving P -waves for the relocated events L2a (diamonds), L2d (squares), L3a (triangles), and L3b (circles) compared with the calculated travel times (lines and crosses) using the initial 1D crustal velocity model. All travel times are reduced by 8.0 km/s and plotted with respect to the minimum recorded travel time. The origin of each event is placed respective to its projected position along the solid line in Figure 1. (c) The same observations as in (b) but with travel times (lines and crosses) predicted from using the refined crustal velocity model and laterally varying Moho model shown in Figure 6 and 7.

Figure 5. The observed P -wave travel times (circles) for events (a) L1e, (b) L1a, (c) L1i, (d) L1j, (e) L1k, and (f) E3b. These sources are located at regional distances to the Hi-CLIMB array, and P_n travel times for these events were used to constrain the P -wave velocity structure of the upper mantle for the region of the Tibetan Plateau. All travel times are reduced by 8.0 km/s and plotted with respect to the minimum recorded travel time. The lines and crosses in each figure show the calculated travel times using the 3D regional velocity model found in this study and shown in Figs. 6 and 7. Horizontal bars highlight the locations of the transition for shoaling of the Moho and northward decrease in P_n speed.

Figure 6. (a) The *P*-velocity model determined in this study showing a 2D transect along the strike of the Hi-CLIMB array shown in Figure 1. Solid lines show velocity contours in km/s. Generally, slower crustal velocities were found beneath the areas of the BNS and IYS. Also, a thicker crust and faster upper mantle velocities were found in the southern area of the plateau beneath the Lhasa terrane. (b) Comparison of the crustal thickness beneath the area of the Hi-CLIMB array determined in this study (gray line) with the interpretation of the major impedance discontinuities (black lines) adapted from the teleseismic imaging by Nowack et al. (2010).

Figure 7. A rendering of the 3D Moho and upper mantle velocity structure found in this study for the region of the Tibetan Plateau. The upper mantle velocities are higher and the Moho deeper beneath the southern portion of the plateau south of the BNS, and upper mantle velocities are lower and the Moho is shallower north of the BNS. However, the area of higher velocities extends farther to the north in the west than in the east and generally follows the trend of the Bangong-Nujiang suture (BNS) as shown by the dashed lines. The Indus-Yarlung suture (IYS) is also shown.

FIGURE 1.

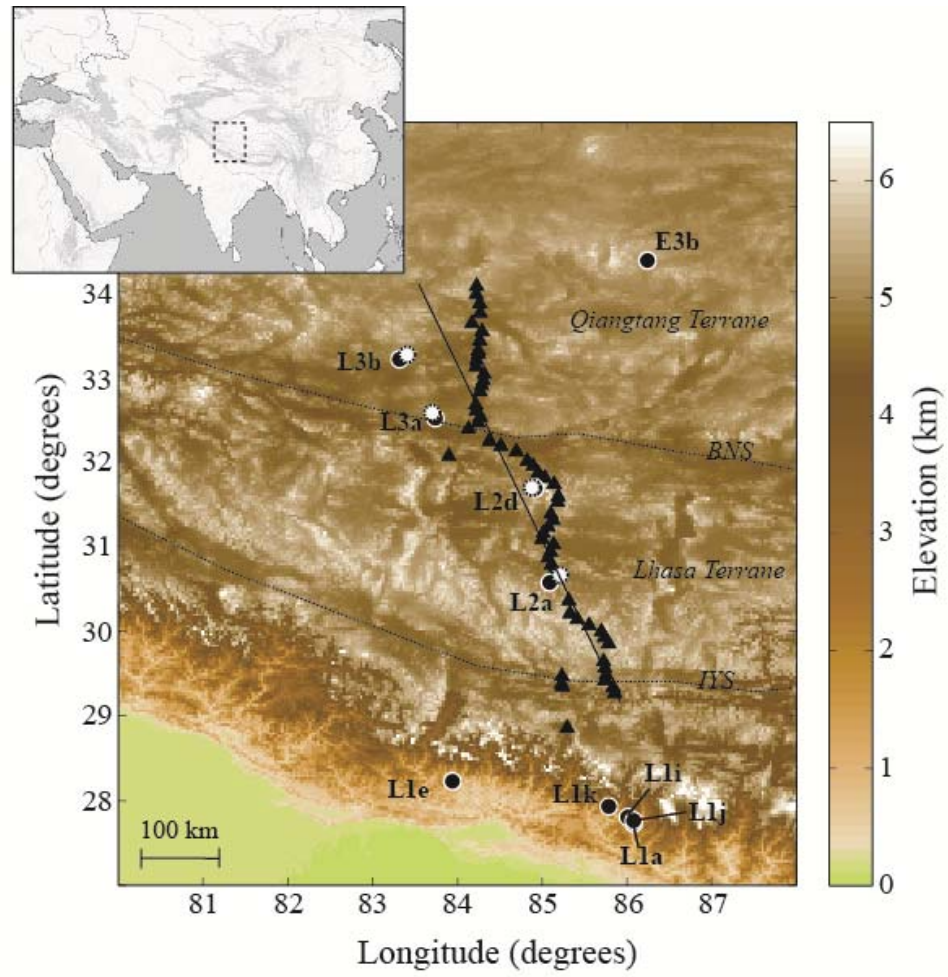


FIGURE 2.

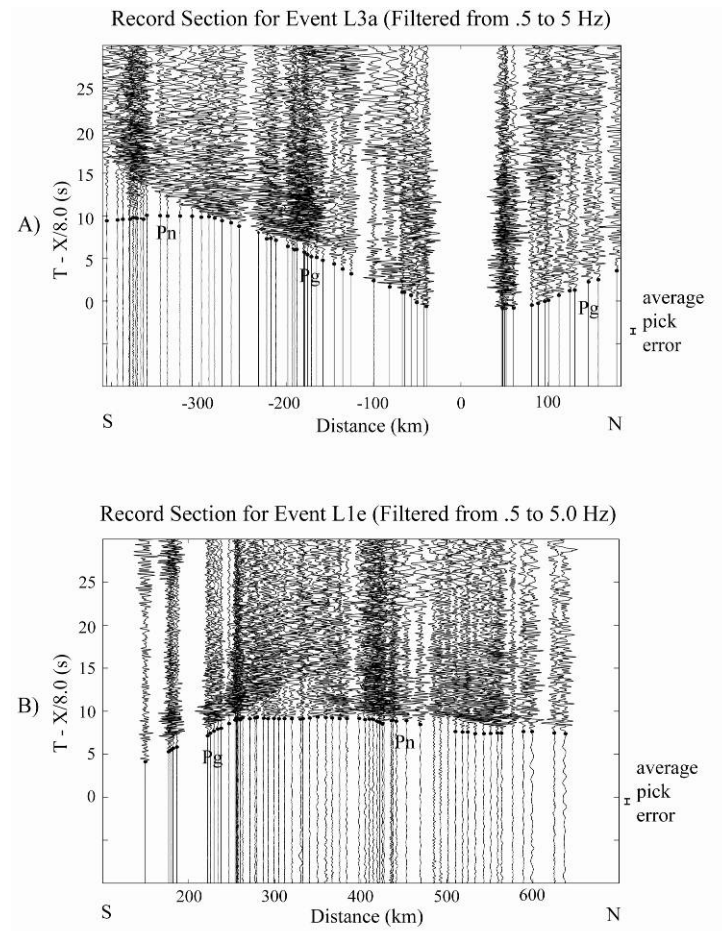


FIGURE 3.

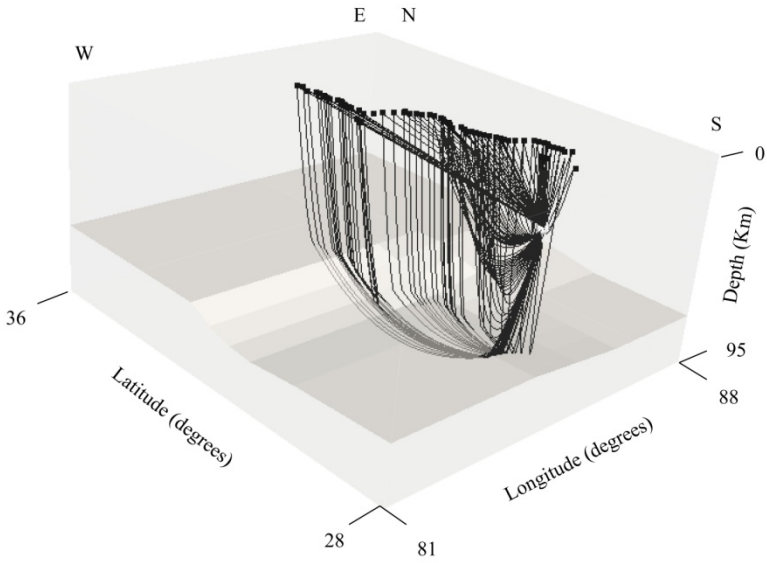


FIGURE 4.

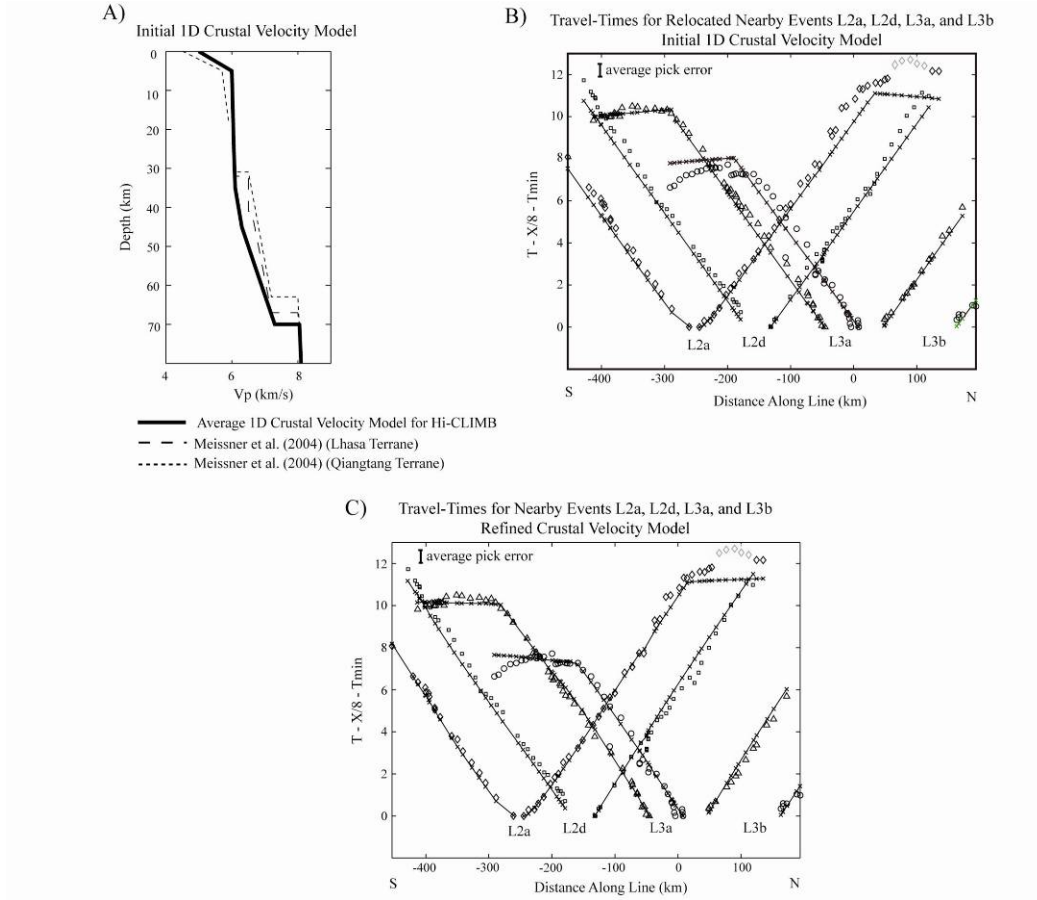


FIGURE 5.

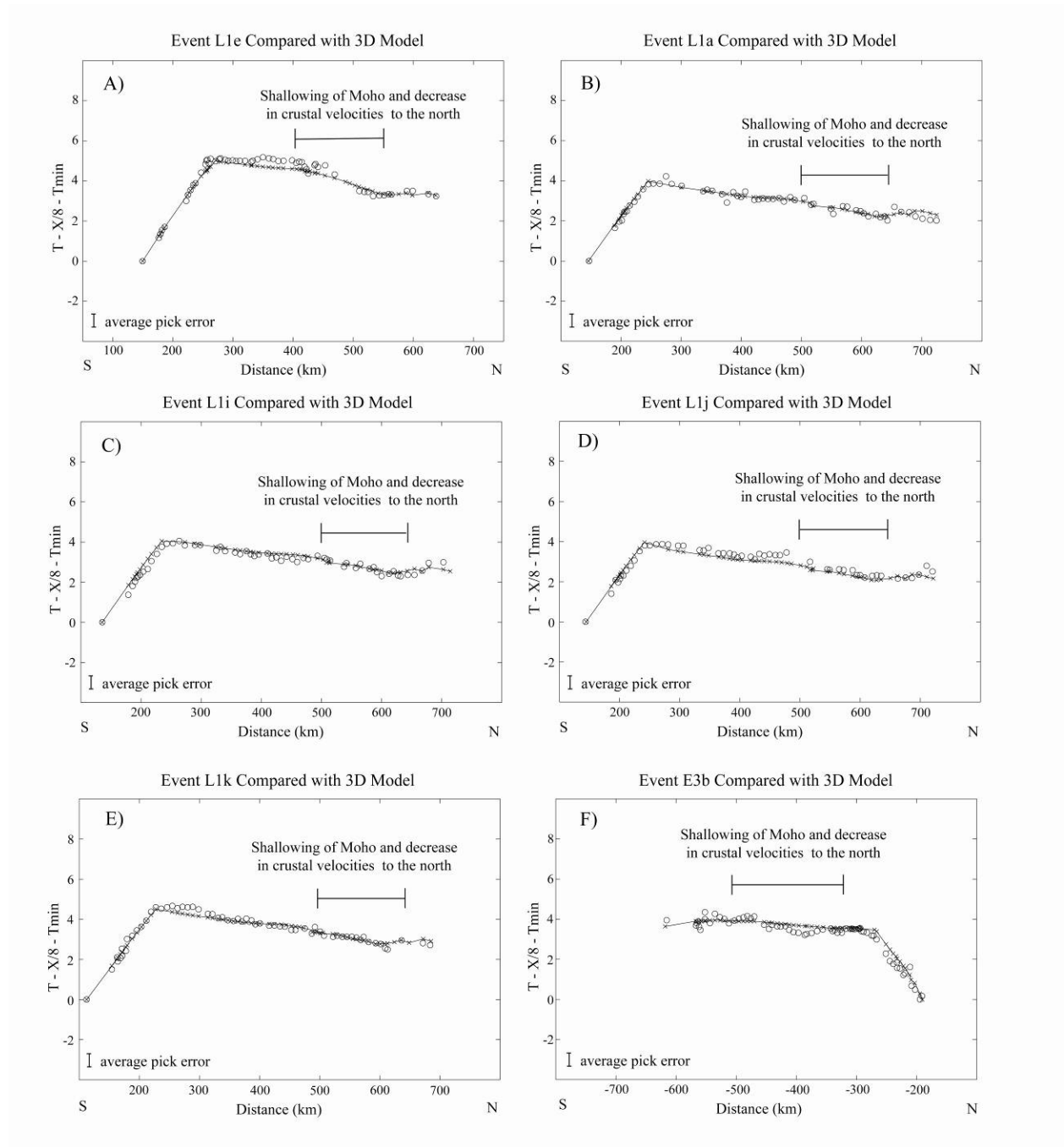


FIGURE 6.

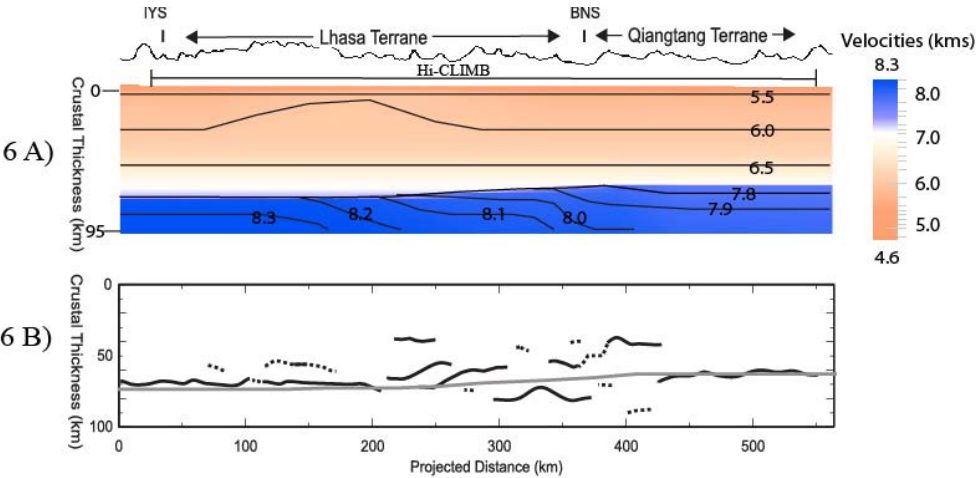
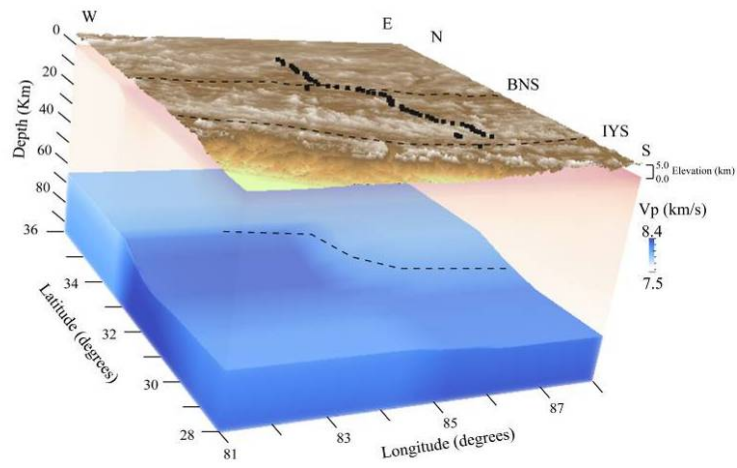


FIGURE 7.



List of Symbols, Abbreviations, and Acronyms

AFRL	Air Force Research Laboratory
BNS	Bangong-Nuijiang Suture in Tibet
CMT	Centroid moment tensor catalog
CRT	Complete Ray Tracing computer package
MPI	Message Passing Interface
PDE	Preliminary Determination of Epicenters catalog
SEM	Spectral element method